Available online at www.sciencedirect.com
ScienceDirect
Comput. Methods Appl. Mech. Engrg. 306 (2016) 452–478
Computer methods in applied mechanics and engineering
www.elsevier.com/locate/cma

An atomistic-to-continuum molecular dynamics: Theory, algorithm, and applications

Shaofan Li[a,*], Shingo Urata[a,b]

[a] *Department of Civil and Environmental Engineering, University of California, Berkeley, CA 94720, USA*
[b] *Innovative Technology Research Center, Asahi Glass Co., Ltd., Yokohama-shi, Kanagawa 230-0045, Japan*

Received 29 December 2015; received in revised form 4 March 2016; accepted 30 March 2016
Available online 13 April 2016

Abstract

To study the connection between atomistic molecular dynamics and macroscale continuum mechanics, we partition the Lagrangian of first-principle molecular dynamics according to its length scales. By doing so, we discover a universal three-scale structure that is embedded in the conventional molecular dynamics formulation, which provides an intrinsic and seamless transition from microscale to macroscale. The multiscale micromorphic molecular dynamics (MMMD) is built on a novel micromorphic multiplicative decomposition that couples a fine scale atomistic dynamics, a mesoscale micromorphic dynamics, and a macroscale particle dynamics of continuum mechanics together in concurrent fashion.

In this work, we discuss the relationship between MMMD and nonlinear continuum mechanics, its computational algorithm, and how to use it to simulate phase transformation under non-equilibrium conditions.

Keywords: Continuum mechanics; Molecular dynamics; Multiscale simulation; Non-equilibrium molecular dynamics; Phase transition

1. Introduction

The state-of-the-art computer and computation technologies have enabled Molecular Dynamics(MD) to simulate evolutions of atomistic material systems with billions of atoms up to a second time duration. The so-called exascale computing technology (e.g. [1]), which provides at least one exaflops 10^{18} s^{-1} computing speed, may soon allow us to carry out first-principle based molecular dynamics simulation of the material systems with size up to cubic micron and maybe even larger volume. With the new technology innovation, such as quantum computer, it is not a far-fetched idea that in a near future we shall soon be able to use Molecular Dynamics in engineering design and analysis for macroscale objects. For instance, we may soon have the computer power (speed and storage) that enable us using Molecular Dynamics to design semiconductor thin films, integrated circuits and silicon chips, smart phones, or even design aircraft turbine engine blades that are working under extreme conditions.

* Corresponding author.
E-mail address: shaofan@berkeley.edu (S. Li).

http://dx.doi.org/10.1016/j.cma.2016.03.048
0045-7825/

This paper attempts to answer a fundamental and theoretical question: can we use the current form of the molecular dynamics to design a macroscale machine or a device component, say a turbine engine blade? The answer is negative! This is because when we design a turbine engine blade we do not (cannot) specify motions of every atom on the surface of the blade! Instead, we design engineering components under specific thermodynamic or statistical conditions, for instance under specific temperature, under given allowable stress or traction state—these are macroscale statistical quantities. One of the main technical challenges of using molecular dynamics in macroscale engineering design is how to apply macroscale boundary conditions to various molecular dynamics ensemble systems, e.g. [2–6]. It is noted that the macroscale mechanical boundary condition is not the fine scale molecular boundary condition for specific atoms at the boundary but the continuum scale boundary condition that we can measure by using macroscale engineering devices.

In fact, one of the focuses of current multiscale simulation research is how to correctly set up the multiscale boundary condition to couple the fine scale atomistic motion with the coarse scale continuum displacement field. In recent years, various multiscale boundary conditions have been proposed e.g. "handshaking condition", or "non-reflection boundary condition", e.g. [7–16] and among others. On the other hand, there have been many efforts to formulate multiscale coarse-grained molecular dynamics. Among them, [17–21] are probably most notable contributions. In particular, in a series work [22–24] Chen et al. proposed a multiscale micromorphic dynamics. In fact, the classical micromorphic continuum theory is also a multiscale theory e.g. [25].

Instead of designing a compatible multiscale interface boundary, in this work, we would like to re-exam the molecular dynamics system itself, which, we believed, has already contained an intrinsic multiscale structure. In early 1980s, Andersen [26] first repartitioned the conventional molecular dynamics Lagrangian, and proposed a multiscale isoenthalpic–isobaric ensemble of molecular dynamics (MD) allowing the volume of a cubic lattice cell to vary. Subsequently, Parrinello and Rahman [27,28] extended Andersen's formalism to the anisotropic case allowing both the volume and the shape of a molecular dynamics (MD) cell to vary, which is in fact an early form of multiscale molecular dynamics. In recent years, there have been renewed interests in revising APR molecular dynamics, e.g. [29–34], which attempted to extend APR MD to non-equilibrium condition or to macroscale simulations.

In a recent work [35–37], by following the Andersen–Parrinello–Rahman approach, the present authors have repartitioned the Lagrangian of the first-principle atomistic molecular dynamics into different scales under the local equilibrium assumption; by doing so, we have discovered that there exists a universal micromorphic multiscale structure in atomistic molecular dynamics, which is an intrinsic mathematical structure of conventional molecular dynamics. The repartitioned first principle molecular dynamics Lagrangian yields three coupled particle dynamics at different scales. The MMMD method allows us: (1) Apply *macroscale boundary conditions* to finite-size molecular dynamics systems, which usually are in the non-equilibrium condition; (2) Calculate non-uniform and inhomogeneous distribution of macroscale field variables of the MD system under applied macroscale boundary conditions, and (3) Bridge microscale molecular dynamics with macroscale continuum mechanics.

In the present work, we are focusing on the following three fundamental and computational issues of MMMD. First by viewing MMMD as a multiscale dynamics from atomistic scale to continuum scale, we discuss what is the relation between MMMD and continuum mechanics. Second, we present a detailed and complete computational algorithms for MMMD, and we discuss the issues on how to implement it in computations. Third, we apply MMMD to simulate the structure phase transition of finite-size crystal systems under applied boundary loadings, which are essentially non-equilibrium boundary flux conditions.

The paper is arranged into five sections. In Section 2, a detailed multiscale partition of first-principle MD Lagrangian and the derivation of the multiscale micromorphic molecular dynamics (MMMD) are presented, in which we focus on the discussion of micromorphic multiplicative decomposition. In Section 3, we derive the dynamical equations of the multiscale micromorphic molecular dynamics (MMMD). In Section 4, a few numerical examples are presented to show how macroscale boundary is applied to simulate crystal structure phase transformation, which validates the proposed multiscale molecular dynamics. Finally, in Section 5, we close the presentation by making few remarks.

2. Multiscale partition of first-principle MD Lagrangian

We first partition the Lagrangian of first-principle molecular dynamics based on domain decomposition and multiscale kinematics of the atom motion.

2.1. Scale decomposition

The first part of multiscale partition is the domain decomposition, i.e. we divide a finite size MD simulation domain into a finite number of supercells or local ensembles, and we choose the α-cell as the representative supercell to illustrate formulation. In the whole simulation domain, we have $\alpha = 1, 2, \ldots, N$ number of cells.

Assume that in the αth cell, there are N_α number of atoms. The position of the center of mass (COM) in this cell is defined as,

$$\mathbf{r}_\alpha(t) = \frac{1}{\sum_i m_i} \sum_i m_i \mathbf{r}_i(t). \tag{1}$$

where $\mathbf{r}_i, i = 1, 2, \ldots, N_\alpha$, is the spatial position of each atom in the current cell configuration. Inversely, we can express the spatial atomic position of ith atom in the αth MD cell as,

$$\mathbf{r}_i = \mathbf{r}_\alpha + \mathbf{r}_{\alpha i}, \quad \alpha = 1, 2, \ldots, N;\ i = 1, 2, \ldots, N_\alpha \tag{2}$$

where $\mathbf{r}_{\alpha i}$ is the relative position for the ith atom in αth cell, and by its definition,

$$\sum_i m_i \mathbf{r}_{\alpha i} = \mathbf{0}, \tag{3}$$

which leads to the condition,

$$\sum_i m_i \mathbf{S}_{i_\alpha} = \mathbf{0}. \tag{4}$$

Here we may use i_α to distinguish the numbering index in different supercells. However, if without confusion, we denote i_α as i or $i \in \alpha$ in the rest of paper.

Now we introduce a so-called micromorphic multiplicative decomposition to describe the relative position of each atom,

$$\mathbf{r}_{\alpha i} = \boldsymbol{\phi}_\alpha \cdot \mathbf{S}_i, \quad \text{and} \quad \boldsymbol{\phi}_\alpha \coloneqq \mathbf{F}_\alpha \cdot \boldsymbol{\chi}_\alpha \tag{5}$$

where $\boldsymbol{\phi}_\alpha$ is the total deformation gradient of the αth supercell; $\mathbf{S}_i$ are the scaled atom position vectors for every atoms inside the αth cell (we use $\mathbf{S}_i$ instead of $\mathbf{S}_{\alpha i}$ for simplicity); the second order tensor $\boldsymbol{\chi}_\alpha$ is the micro deformation tensor of the αth cell, and its physical meaning may be interpreted as the shape tensor of αth cell,

$$\boldsymbol{\chi}_\alpha(t)\mathbf{S}_i(t) = \xi_i(t)\mathbf{a}(\mathbf{t}) + \eta_i(t)\mathbf{b}(\mathbf{t}) + \zeta_i(t)\mathbf{c}(\mathbf{t}), \quad i = 1, 2, \ldots, N_\alpha$$

where $\mathbf{a}$, $\mathbf{b}$, and $\mathbf{c}$ are the MD cell edge vectors, and ξ_i, η_i, and ζ_i are the components of the local position vector $\mathbf{S}_i$ projecting onto the MD cell edges. They can be expressed into the following matrix form,

$$\boldsymbol{\chi}_\alpha(t) = \begin{pmatrix} a_x(t) & b_x(t) & c_x(t) \\ a_y(t) & b_y(t) & c_y(t) \\ a_z(t) & b_z(t) & c_z(t) \end{pmatrix}, \qquad \mathbf{S}_i(t) = \begin{pmatrix} \xi_i(t) \\ \eta_i(t) \\ \zeta_i(t) \end{pmatrix}.$$

If we place the center of the supercell at the origin of the local coordinate, the components of the local position vector of $\mathbf{S}_i$ oscillate in the range,

$$-0.5 \le \xi_i(t), \eta_i(t), \zeta_i(t) \le 0.5,$$

which characterizes the internal degrees of freedom of atom motions. When the total number of atoms increases, the motion of $\mathbf{S}_i$ may become chaotic. Therefore, we refer the local position vectors $\mathbf{S}_i$ as the statistical variables. Borrowing the terminology in macroscale continuum mechanics, we call the assemble of $\{\mathbf{S}_i\}$ as the statistical parametric configuration, i.e. $\mathbf{S}_i \in \mathcal{B}_S$.

The key part of the multiplicative micromorphic decomposition is the introduction of a coarse scale deformation gradient $\mathbf{F}_\alpha = \mathbf{F}_\alpha(\{\mathbf{r}_\beta\})$ that is determined by the overall motion of all centers of mass of every cells, which

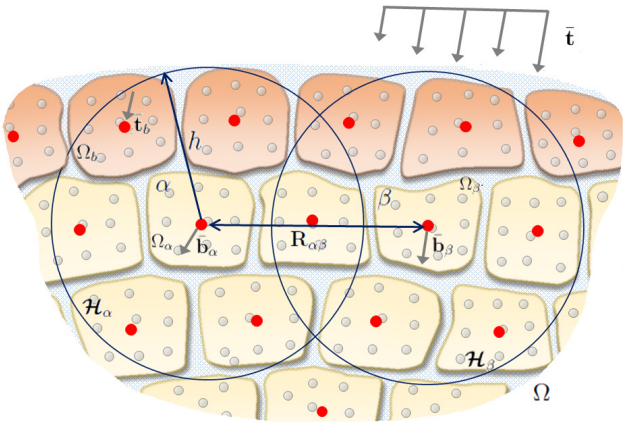

Fig. 1. Schematic illustration of supercell domain decomposition; the dark points are centers of mass of supercells that may be subjected external body force; the dark supercells are boundary cells that may be subjected external traction. The center of mass for each supercell has a support $\mathcal{H}_\alpha$ that contains some other centers of mass of adjacent supercells.

are completely determined by the spatial distribution of centers of mass (implied by the dependence of $\{\mathbf{r}_\beta\}$) of all cells.

Fig. 1 shows a schematic spatial cell division and the corresponding distribution of centers of mass. $\mathbf{F}_\alpha$ together with $\boldsymbol{\chi}_\alpha$ constitute the total deformation gradient $\boldsymbol{\phi}_\alpha$, and $\mathbf{F}_\alpha$ are determined by the distribution of $\{\mathbf{r}_\alpha\}$. For example, we can determine $\mathbf{F}_\alpha$ by using the approach adopted in the reproducing kernel particle method [38] or the state-based peridynamics [39].

Denote

$$\mathbf{r}_{\alpha\beta}(t) = \mathbf{r}_\beta(t) - \mathbf{r}_\alpha(t), \qquad \mathbf{R}_\alpha := \mathbf{r}_\alpha(0), \quad \text{and} \quad \mathbf{R}_{\alpha\beta} = \mathbf{R}_\beta - \mathbf{R}_\alpha, \tag{6}$$

where the Greek subscripts are indices of the centers of mass of MD cells. As shown in Fig. 1, each supercell center has a compact support, say $\mathcal{H}_\alpha$ for the cell α. We can then construct the so-called moment matrix or shape tensor for the cell center α by calculating following discrete sum over the other cell centers inside the support $\mathcal{H}_\alpha$ (See [38]),

$$\mathbf{M}_\alpha := \sum_{\beta=1}^{N_h} \omega(|\mathbf{R}_{\alpha\beta}|)\mathbf{R}_{\alpha\beta} \otimes \mathbf{R}_{\alpha\beta}\Omega_{\beta 0}, \tag{7}$$

where $\otimes$ is the tensor product operator; N_h is the number of supercell centers inside $\mathcal{H}_\alpha$; $\Omega_{\beta 0}$ is the volume of the βth cell in the referential configuration $\mathcal{B}_R$, and $\omega(|\mathbf{R}_{\alpha\beta}|)$ is a localized positive window function.

To construct the macroscale deformation gradient tensor, we first define a two-point second order tensor by the following discrete sum,

$$\mathbf{N}_\alpha := \left(\sum_{\beta=1}^{N_h} \omega(|\mathbf{R}_{\alpha\beta}|)\mathbf{r}_{\alpha\beta} \otimes \mathbf{R}_{\alpha\beta}\Omega_{\beta 0}\right), \tag{8}$$

where $\mathbf{r}_{\alpha\beta} \in \mathcal{B}_r$ and $\mathbf{R}_{\alpha\beta} \in \mathcal{B}_R$. Considering the Cauchy–Born rule [40], we have,

$$\mathbf{r}_{\alpha\beta} = \mathbf{F}_\alpha \cdot \mathbf{R}_{\alpha\beta} \;\rightarrow\; \mathbf{N}_\alpha = \mathbf{F}_\alpha \cdot \mathbf{M}_\alpha,$$

and then we can derive the coarse scale deformation gradient as

$$\mathbf{F}_\alpha = \left(\sum_{\beta=1}^{N_h} \omega(|\mathbf{R}_{\alpha\beta}|)\mathbf{r}_{\alpha\beta} \otimes \mathbf{R}_{\alpha\beta}\Omega_{\beta 0}\right) \cdot \mathbf{M}_\alpha^{-1}. \tag{9}$$

where $\omega(|\mathbf{R}_{\alpha\beta}|)$ is a localized positive window function, and a common choice is the Gaussian function,

$$\omega_h(\mathbf{x}) = \frac{1}{(\pi h^2)^{d/2}} \exp\Big(-\frac{\mathbf{x}\cdot\mathbf{x}}{h^2}\Big), \tag{10}$$

here d is the number of space dimension, and h is the radius of the support. Obviously, $\mathbf{F}_\alpha$ depends on the relative positions of all other atoms in the support of the α-atom, i.e. Ω_α. Note that in the configurations $\mathcal{B}_R$ and $\mathcal{B}_I$ the center of the supercell occupies the same position, i.e. $\mathbf{R}_\alpha \equiv \mathcal{R}_\alpha$, but not for each atom, i.e. $\mathbf{R}_{\alpha i} \neq \mathcal{R}_{\alpha i}$.

At the beginning of the coarse scale deformation, the initial position of the supercell center $\mathbf{r}_\alpha(0) = \mathbf{R}_\alpha$, therefore,

$$\mathbf{F}_\alpha = \left(\sum_{\beta=1}^{N_h} \omega(|\mathbf{R}_{\alpha\beta}|)\mathbf{r}_{\alpha\beta}\otimes\mathbf{R}_{\alpha\beta}\Omega_{\beta 0}\right)\cdot\mathbf{M}_\alpha^{-1} = \left(\sum_{\beta=1}^{N_h} \omega(|\mathbf{R}_{\alpha\beta}|)\mathbf{R}_{\alpha\beta}\otimes\mathbf{R}_{\alpha\beta}\Omega_{\beta 0}\right)\cdot\mathbf{M}_\alpha^{-1} = \mathbf{I},$$

where $\mathbf{I}$ is the unit of second order tensor.

Initially, the supercell shape tensor, $\boldsymbol{\chi}_0$, which is spanned by the three edges of the MD cell, $\mathbf{a}(0)$, $\mathbf{b}(0)$, and $\mathbf{c}(0)$, may be expressed as,

$$\boldsymbol{\chi}_0 \coloneqq \boldsymbol{\chi}(0) = [\mathbf{a}(0), \mathbf{b}(0), \mathbf{c}(0)].$$

For all the atoms in a representative MD cell, say the αth cell, its referential position are defined as

$$\mathbf{R}_i \coloneqq \mathbf{R}_\alpha + \mathbf{R}_{\alpha i}, \quad \text{with } \mathbf{R}_{\alpha i} = \boldsymbol{\chi}_0\mathbf{S}_i. \tag{11}$$

In the rest of this paper, we refer this molecular configuration as the referential configuration $\mathcal{B}_R$. One can find that this definition is consistent with kinematic assumption,

$$\mathbf{r}_i = \mathbf{r}_\alpha + \mathbf{r}_{\alpha i} = \mathbf{r}_\alpha + \mathbf{F}_\alpha\cdot\boldsymbol{\chi}_\alpha\cdot\mathbf{S}_i. \tag{12}$$

Based on Eq. (12), we may define an intermediate referential configuration,

$$\mathcal{R}_i = \mathbf{R}_\alpha + \mathcal{R}_{\alpha i} = \mathbf{R}_\alpha + \boldsymbol{\chi}_\alpha(t)\cdot\mathbf{S}_i, \tag{13}$$

so that the coarse scale deformation gradient is a continuum scale deformation gradient.

In the proposed multiscale method, we have introduced four different configurations in a representative cell α: (1) The spatial configuration, i.e. $\mathcal{B}_c(\mathbf{r})$-configuration, in which $\mathbf{r}_i \in \Omega_\alpha$; (2) the intermediate equilibrium configuration, i.e. $\mathcal{B}_I(\mathcal{R})$-configuration; (3) the referential equilibrium configuration, i.e. $\mathcal{B}_I(\mathbf{R})$-configuration, in which $\mathbf{R}_i \in \Omega_{\alpha 0}$, and (4) the statistical configuration $\mathcal{B}_S$, in which the scaled atom coordinate $\mathbf{S}_i$ are primary variables. Fig. 2 shows a deformation map that connects these four configuration spaces.

Since for the monoatom systems $\sum_i m_i\mathbf{S}_i = 0$ and $\mathbf{S}_i$ are oscillating in the range $-0.5 \le \mathbf{S}_i \le 0.5$, i.e. $\|\mathbf{S}_i\| < 1$, as atoms oscillate around their equilibrium positions, we may interpret $\mathbf{S}_i$ as a statistical variable. For a given macroscale kinematic variable or point, $\mathbf{r}_\alpha(t)$ (the center of cell), there are many sets of $\{\mathbf{S}_i\}$ corresponding to it, and this is the case because as long as $\sum_i m_i\mathbf{S}_i = 0$ satisfies. Therefore, a given macroscale material point $\mathbf{r}_\alpha(t)$ does not correspond to a single set of $\{\mathbf{S}_i\}$ in a unique one-to-one manner, i.e. such correspondence is not unique. This makes sense because in statistical thermodynamics a macroscale state $\mathbf{r}_\alpha$ corresponds to many microstates $\{\mathbf{S}_i\}$, and a microstate is determined by the distribution of statistical variable $\mathbf{S}_i$.

It may be also noted that on the configuration spaces $\mathcal{B}_I$, $\mathcal{B}_R$, the center of mass coordinate are the same, i.e. $\mathbf{R}_\alpha$, whereas the configuration space $\mathcal{B}_S$ is defined cell by cell, and the coordinate of the center of mass of each cell is zero.

Remark 2.1. It may be noted that in PR-MD [32], $\mathbf{F} \coloneqq \boldsymbol{\chi}\cdot\boldsymbol{\chi}_0^{-1}$ with $\boldsymbol{\chi}_0 \coloneqq \langle\boldsymbol{\chi}(t)\rangle$, which is a mesoscale variable, i.e. it has the same time and length scales as the mesoscale variable $\boldsymbol{\chi}(t)$. A shortcoming for such approach is that the definition of $\boldsymbol{\chi}_0$ is posterior. Whereas in MMMD, $\mathbf{F}_\alpha$ are solely determined by the global position of the centers of mass of supercells, therefore they are coarse scale variables.

A pictorial illustration of four physical configurations is displayed in Fig. 3, where physical interpretations of different kinematic mappings at different scales are graphically illustrated. In passing we note that the continuum compatibility condition is a macroscale condition, and at both microscale and mesoscale this condition is not necessarily satisfied. For crystalline solids, this may be linked to the defect states or quasi-crystal states. Even though

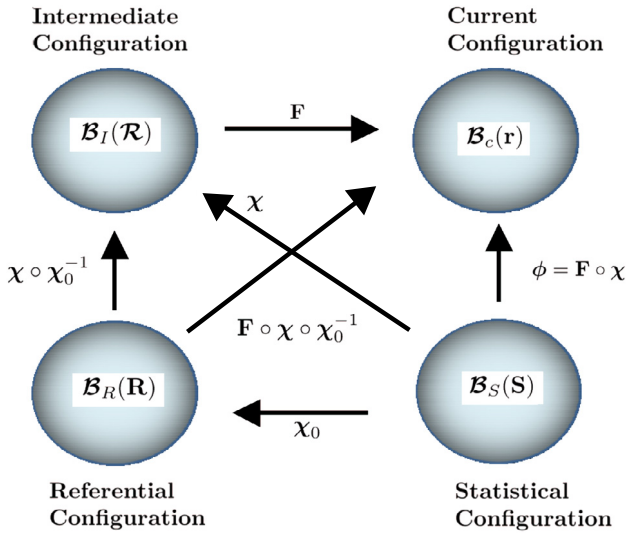

Fig. 2. Deformation map that connects four different kinematic configuration spaces: (1) statistical configuration; (2) referential configuration; (3) intermediate configuration, and (4) current configuration.

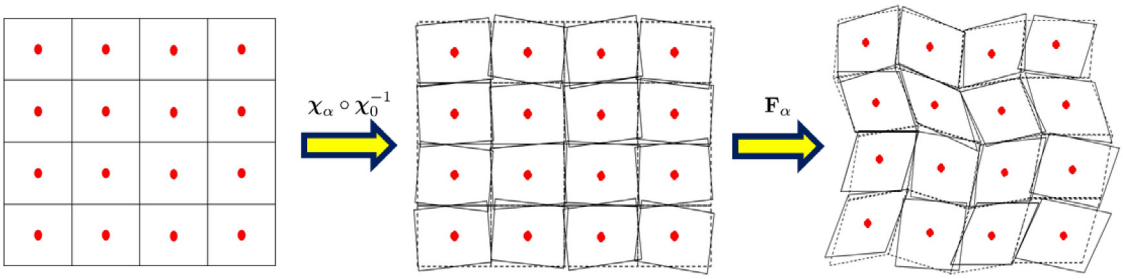

(a) $\mathcal{B}_R(\mathbf{R})$. (b) $\mathcal{B}_I(\mathcal{R})$. (c) $\mathcal{B}_c(\mathbf{r})$.

Fig. 3. Cell Deformation in different configurations: (a) The original undeformed system which is divided into several unit cells. The atomic positions are given by $\mathbf{R}_i$. The solid circles represent the centers of mass. (b) The cells (dashed parallelograms) further undergoes microscale deformation $\boldsymbol{\chi}_\alpha$ around their own center of mass separately without connection (with the cell center fixed). This is because that continuity may not be valid at fine scale. (c) The configuration undergoes macroscale deformation $\mathbf{F}_\alpha$, i.e. now the cell centers start to move. Notice that the continuity is a macroscale concept. Based on this concept, we can use the positions of all cell centers to construct, e.g. interpolate, a coarse scale displacement field.

the referential configuration is not essential in the fine scale calculations, but its information is needed in coarse scale computations. To clearly specify displacement decomposition at each scale, we consider the following atomic position decomposition,

$$\mathbf{r}_i = \mathbf{r}_\alpha + \mathbf{r}_{\alpha i} \;\Rightarrow\; \mathbf{r}_i = \mathbf{r}_\alpha + \mathbf{F}_\alpha \cdot \mathcal{R}_{\alpha i} = \mathbf{r}_\alpha + \mathbf{F}_\alpha \cdot \boldsymbol{\chi}_\alpha \cdot \mathbf{S}_i, \tag{14}$$

where

$$\mathcal{R}_{\alpha i} = \boldsymbol{\chi}_\alpha \cdot \mathbf{S}_i.$$

These relations are schematically illustrated in Fig. 4. Subsequently, we can decompose the atomistic displacement into three different scales,

$$\bar{\mathbf{u}} = \mathbf{r}_\alpha - \mathbf{R}_\alpha; \qquad \tilde{\mathbf{u}}_i = \Big(\mathbf{F}_\alpha \cdot \boldsymbol{\chi}_\alpha - \boldsymbol{\chi}_\alpha\Big)\mathbf{S}_i, \quad \text{and} \quad \mathbf{u}'_i = \Big(\boldsymbol{\chi}_\alpha - \boldsymbol{\chi}_{\alpha 0}\Big)\mathbf{S}_i, \tag{15}$$

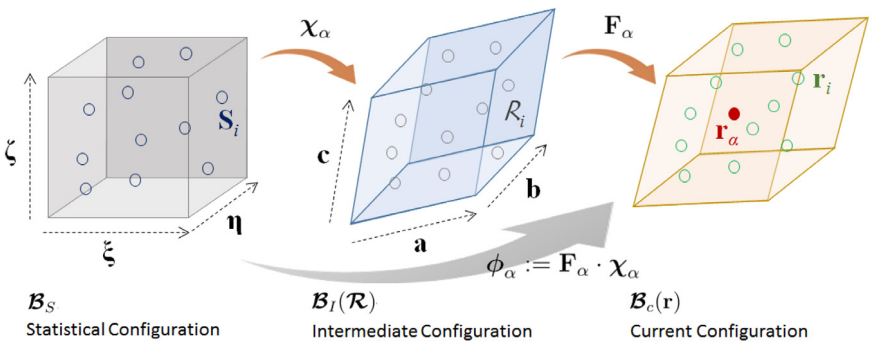

Fig. 4. Schematic illustrations of relations among (I) statistical configuration, (II) intermediate configuration and (III) current configuration. See the definitions of coordinations, $\mathbf{s}_i$, $\mathbf{r}_i$, and $\mathbf{r}_\alpha$ in Eq. (14).

where $\bar{\mathbf{u}}$, $\tilde{\mathbf{u}}_i$, $\mathbf{u}'_i$ denote macroscale, mesoscale, and microscale displacements. Apparently, three of them together constitute the total displacement $\mathbf{u}_i$, which can be expressed as,

$$\mathbf{u}_i = \bar{\mathbf{u}} + \tilde{\mathbf{u}}_i + \mathbf{u}'_i = \mathbf{r}_i - \mathbf{R}_i. \tag{16}$$

In the scale decomposition, we select three independent kinematic variables, $\{\mathbf{S}_i, \boldsymbol{\chi}_\alpha, \text{and } \mathbf{r}_\alpha\}$, to represent three different scales. The novelty of the proposed multiscale decomposition is the **Multiplicative Multiscale Decomposition**,

$$\boldsymbol{\phi}_\alpha = \mathbf{F}_\alpha \cdot \boldsymbol{\chi}_\alpha. \tag{17}$$

This decomposition is in sharp contrast to the addictive multiscale decomposition proposed by Wagner and Liu [8]. The total deformation gradient $\boldsymbol{\phi}_\alpha$ consists of a macroscale deformation gradient $\mathbf{F}_\alpha$ and a micromorphic (meso) deformation gradient $\boldsymbol{\chi}_\alpha$. The macroscale deformation gradient at a local position is completely determined by the local distribution of the supercell centers, which can be quantified, for example, by Eq. (9). On the other hand, the microscale deformation gradient, which is often called as the micro-deformation in the literature of micromorphic theory, is an independent mesoscale field variable that quantifies the independent supercell rotation or microscale deformation. The macro deformation $\mathbf{F}_\alpha$ may be considered to be **Long-range order**, whereas the micro-deformation $\boldsymbol{\chi}_\alpha$ may be considered to be **Short-range order**.

Remark 2.2. 1. The main objective of MMMD is to study non-equilibrium molecular dynamics process. Most of conventional molecular dynamics are intended for equilibrium canonical ensembles such as NVE, NVT, or NPH, etc., in which either the stress, or volume, or temperature, or enthalpy, or a given thermodynamic variable is fixed over the whole system, by which, we mean, it is under the maximum entropy condition with certain specific thermodynamics variable being fixed or being constant. For non-equilibrium systems, the system's entropy is not at the maximum value, and the evolutions of the systems are driven by the boundary thermodynamics flux, such as heat flux, linear momentum flux (traction), or energy flux, etc. These boundary conditions can be specified by prescribed motions of each and every atom on the boundary, or by simply specifying the statistical quantity of the flux, which we may call it as the macroscale boundary condition. An immediate question is how? A key assumption adopted in this work is the local equilibrium assumption (LEA), which means that a local equilibrium state may be attained in each local micromorphic cell during a small time interval. For instance, even if the whole system, the stress is not constant, but in an individual cell, the stress may become constant at a specific moment. This will allow us to calculate spatial stress distribution as well as specify the stress state of every boundary cells so that we can prescribe boundary traction as a statistical quantity of linear momentum flux in each boundary cell. **2.** The micromorphic cell division is a Lagrangian division, meaning that each cell has a fixed (controlled) number of atoms (N_α), or it is a local equilibrium NσH or a local NSH ensemble, but not a fixed volume Eulerian cell. Moreover, it is also different from the Lagrangian type control volume ensemble such as a local NVT cell [41,42]. It must be noted that the multiscale micromorphic molecular dynamics proposed in this paper excludes the cases that have long range random molecular diffusion, such as molecular Brownian motion in liquids and gases.

Both the Lagrangian division as well as MMMD formulation are derived from first principle, and it does add additional topological constraints onto the original first-principle Lagrange. Rather, it is a device to extrapolate the

statistical variables of a MD system in a non-equilibrium setting. Therefore, we allow cell overlap, penetration, as well as having gaps, if that is what indeed happen in the original atomistic system. This philosophy is illustrate in Fig. 3.

2.2. Statistical conditions

Before deriving the dynamic equations of MMMD, we first exam the kinetic energy of the αth cell:

$$\begin{aligned} K_\alpha &= \frac{1}{2}\sum_i m_i \dot{\mathbf{r}}_i \cdot \dot{\mathbf{r}}_i = \frac{1}{2}\sum_i m_i (\dot{\mathbf{r}}_\alpha + \dot{\boldsymbol{\phi}}_\alpha \cdot \mathbf{S}_i + \boldsymbol{\phi}_\alpha \cdot \dot{\mathbf{S}}_i) \cdot (\dot{\mathbf{r}}_\alpha + \dot{\boldsymbol{\phi}}_\alpha \cdot \mathbf{S}_i + \boldsymbol{\phi}_\alpha \cdot \dot{\mathbf{S}}_i) \\ &= \underbrace{\frac{M_\alpha}{2}\dot{\mathbf{r}}_\alpha \cdot \dot{\mathbf{r}}_\alpha}_{K_1} + \underbrace{\frac{1}{2}\dot{\boldsymbol{\phi}}_\alpha^T \dot{\boldsymbol{\phi}}_\alpha \sum_i m_i \mathbf{S}_i \otimes \mathbf{S}_i}_{K_2} + \underbrace{\frac{1}{2}\sum_i m_i \dot{\mathbf{S}}_i \cdot \mathbf{C} \cdot \dot{\mathbf{S}}_i}_{K_3} \\ &\quad + \underbrace{\frac{1}{2}\dot{\boldsymbol{\phi}}_\alpha^T \boldsymbol{\phi}_\alpha \sum_i m_i \mathbf{S}_i \otimes \dot{\mathbf{S}}_i + \frac{1}{2}\boldsymbol{\phi}_\alpha^T \dot{\boldsymbol{\phi}}_\alpha \sum_i m_i \dot{\mathbf{S}}_i \otimes \mathbf{S}_i}_{K_4}, \end{aligned} \tag{18}$$

where $M_\alpha = \sum_i m_i$ is the mass of the cell, and $\mathbf{C} = \boldsymbol{\phi}_\alpha^T \boldsymbol{\phi}_\alpha$ is the multiscale right Cauchy–Green tensor.

Assuming that the spatial and temporal spaces are statistical isotropic and homogeneous, we postulate the following statistical condition,

$$\mathbf{J}_\alpha^S = \sum_i m_i \mathbf{S}_i \otimes \mathbf{S}_i = \boldsymbol{\chi}_{\alpha 0}^{-1} \cdot \mathbf{J}_\alpha \cdot \boldsymbol{\chi}_{\alpha 0}^{-T} = \text{constant tensor}, \tag{19}$$

where

$$\mathbf{J}_\alpha = \sum_i m_i \mathbf{R}_{\alpha i} \otimes \mathbf{R}_{\alpha i} \tag{20}$$

is a second order tensor that is similar to the moment of inertia tensor of the cell in referential space. In mechanics, the moment of inertia tensor of a rigid body is defined as,

$$\mathbf{I}_{Euler} \coloneqq \int_V \rho\Big(\|\mathbf{R}\|^2 \mathbf{I}^{(2)} - \mathbf{R} \otimes \mathbf{R}\Big) dV$$

where ρ is mass density, and $\mathbf{I}^{(2)}$ is the second order unit tensor. It is obvious that $\mathbf{I}_{Euler}$ is dependent on both the shape and size of the rigid body. Similarly the tensor $\mathbf{J}_\alpha$ is also dependent on both the shape and size of the micromorphic MD cell. On the other hand, the second order tensor $\mathbf{J}_\alpha^S$ is not dependent on the MD cell size and shape. In fact $\mathbf{J}_\alpha^S$ is the push-back of $\mathbf{J}_\alpha$ [43], and $\boldsymbol{\chi}_{\alpha 0} = \boldsymbol{\chi}(0)$ is a constant second order tensor, i.e. the geometric shape tensor of the original cell.

We can replace the discrete summation (19) with a continuous integration, i.e.

$$\mathbf{J}_\alpha^S = \int_\omega \rho \mathbf{S} \otimes \mathbf{S} d\omega_S \tag{21}$$

where ω is the volume of a unit cube. Let $\mathbf{E}_I$ be the principal axes of $\mathbf{J}_\alpha^S$. We can then have the spectral decomposition of $\mathbf{J}_\alpha^S$,

$$\mathbf{J}_\alpha^S = \sum_{I=1}^{3} \left(\int_\omega \rho S_I^2 d\omega \right) \mathbf{E}_I \otimes \mathbf{E}_I. \tag{22}$$

If we postulate that $\mathbf{J}_\alpha^S$ is a spherical tensor, we have

$$\int_\omega \rho S_1^2 d\omega = \int_\omega \rho S_2^2 d\omega = \int_\omega \rho S_3^2 d\omega =: W_\alpha. \tag{23}$$

It should be noted that the supercell is not a necessarily unit cube, and it is related to the physical shape of the lattice representative cell. Therefore, the related Euler's moment of inertia tensor, $\mathbf{I}_{Euler}$ is in general anisotropic. On the other hand, the moment tensor $\mathbf{J}_\alpha^S$ in (21) is defined in the statistical configuration. The assumption that $\mathbf{J}_\alpha^S$ is a spherical tensor is based on the general ergodicity postulate that the space and time that a molecular dynamics simulation is involved are statistical isotropic and homogeneous, which is one of the fundamental hypothesis in statistical physics and molecular physics. Note that we are discussing a quantity in a statistical configuration $\mathcal{B}_S$, not the lattice configuration $\mathcal{B}_R$ and $\mathcal{B}_I$ nor the current configuration $\mathcal{B}_c$. The anisotropy of a material in the lattice space is not in conflict with the ergodic assumption stated here.

For this reason, Parrinello and Rahman [28] assumed that

$$K_2 = \frac{1}{2} W_\alpha \mathrm{Trace}(\dot{\boldsymbol{\phi}}_\alpha^T \dot{\boldsymbol{\phi}}_\alpha). \tag{24}$$

We call the expression (19) as the **First statistical condition** of APR-MD; and the expression (23) as the **Second statistical condition** of APR-MD.

Next we consider the fourth term of the kinetic energy K_4. Since we may label $\mathbf{S}_i$ statistical variables, one may find that $\mathbf{J}_\alpha^S$ is in fact a tensorial autocorrelation function of statistical positions,

$$\mathbf{J}^S(\tau) = \langle \mathbf{S}_i(t) \otimes \mathbf{S}_i(t+\tau) \rangle := \sum_i m_i \mathbf{S}_i(t) \otimes \mathbf{S}_i(t+\tau). \tag{25}$$

We can prove that the autocorrelation tensor is an even function of τ, if $\mathbf{J}^S$ is spherical. This implies the derivation at the origin $\tau = 0$ is zero. Hence,

$$\frac{d}{d\tau} \mathbf{J}_\alpha^S|_{\tau=0} = \sum_i m_i \mathbf{S}_i(t) \otimes \dot{\mathbf{S}}_i(t) = \mathbf{0}, \tag{26}$$

and similarly,

$$\sum_i m_i \dot{\mathbf{S}}_i(t) \otimes \mathbf{S}_i(t) = \mathbf{0}. \tag{27}$$

Eqs. (26) and (27) imply that $K_4 = \mathbf{0}$. In fact, the Second statistical condition states that $\mathbf{J}_\alpha^S$ is a spherical tensor, which implies that

$$\mathbf{J}_\alpha^S(\tau) = \langle \mathbf{S}_i(t) \otimes \mathbf{S}_i(t+\tau) \rangle = \sum_i m_i \mathbf{S}_i(t) \otimes \mathbf{S}_i(t+\tau) = \left(\sum_i m_i S_i(t) S_i(t+\tau) \right) \mathbf{E}_I \otimes \mathbf{E}_I$$

where $\mathbf{E}_I$, $I = 1, 2, 3$ are the basis of a Cartesian coordinate. It then follows,

$$\begin{aligned} \mathbf{J}_\alpha^S(-\tau) &= \langle \mathbf{S}_i(t) \otimes \mathbf{S}_i(t-\tau) \rangle = \sum_i m_i \mathbf{S}_i(t) \otimes \mathbf{S}_i(t-\tau) \\ &= \left(\sum_i m_i S_i(t) S_i(t-\tau) \right) \mathbf{E}_I \otimes \mathbf{E}_I = \left(\sum_i m_i S_i(t+\tau) S_i(t) \right) \mathbf{E}_I \otimes \mathbf{E}_I \\ &= \langle \mathbf{S}_i(t) \otimes \mathbf{S}_i(t+\tau) \rangle = \mathbf{J}_\alpha^S(\tau). \end{aligned}$$

Remark 2.3. Mathematically, the Second statistical closures (26) and (27) provide six equations. Together with the three constraint equations provided by the First statistical closure, they are the nine conditions that are needed to ensure that the variables $\boldsymbol{\chi}_\alpha$ and $\mathbf{S}_i$ are independent. Thus, we now understand why APR-MD is not an approximation of first principle molecular dynamics, but an exact and alternative and thermodynamically partition of first principle molecular dynamics.

Utilizing the two statistical conditions, we can write the Lagrangian of the MMMD system as,

$$\mathcal{L}_m = \frac{1}{2}\sum_\beta M_\beta \dot{\mathbf{r}}_\beta \cdot \dot{\mathbf{r}}_\beta + \frac{1}{2}\sum_\beta \mathbf{J}^S_\beta : (\dot{\boldsymbol{\phi}}^T_\beta \dot{\boldsymbol{\phi}}_\beta) + \frac{1}{2}\sum_\beta \sum_i m_i \dot{\mathbf{S}}_i \cdot \mathbf{C}_\beta \cdot \dot{\mathbf{S}}_i - \frac{1}{2}\sum_\beta \sum_\gamma \sum_{i\in\beta, j\in\gamma} V(r_{ij}) - \sum_\beta \sum_{i\in\beta} \mathbf{b}_i \cdot \mathbf{r}_i \tag{28}$$

where β, γ are cell number indices, and the abbreviation $i \in \beta$ means that the ith atom belongs to the βth cell. $\mathbf{C}_\beta := \boldsymbol{\phi}^T_\beta \boldsymbol{\phi}_\beta$ is the multiscale right Cauchy–Green tensor for total deformation.

In the rest of the paper, we choose three independent field variables, $\mathbf{r}_\alpha, \boldsymbol{\phi}_\alpha$, and $\mathbf{S}_i$ representing kinematic variables for three scales, instead of the set of original variables $\mathbf{r}_\alpha, \boldsymbol{\chi}_\alpha, \mathbf{S}_i$, which will be equivalent each other. Thus $\mathcal{L}_m = \mathcal{L}_m(\mathbf{r}_\alpha, \boldsymbol{\phi}_\alpha, \mathbf{S}_i)$. The equations of motion are stated as

$$\frac{d}{dt}\frac{\partial \mathcal{L}_m}{\partial \dot{\mathbf{r}}_\alpha} - \frac{\partial \mathcal{L}_m}{\partial \mathbf{r}_\alpha} = 0; \qquad \frac{d}{dt}\frac{\partial \mathcal{L}_m}{\partial \dot{\boldsymbol{\phi}}_\alpha} - \frac{\partial \mathcal{L}_\alpha}{\partial \boldsymbol{\phi}_\alpha} = 0, \quad \text{and} \quad \frac{d}{dt}\frac{\partial \mathcal{L}_m}{\partial \dot{\mathbf{S}}_i} - \frac{\partial \mathcal{L}_\alpha}{\partial \mathbf{S}_i} = 0. \tag{29}$$

3. Multiscale micromorphic molecular dynamics (MMMD)

In this section, we shall derive the dynamic equations for multiscale micromorphic molecular dynamics.

3.1. Coarse scale dynamic equation

We start by deriving some relations that are needed in subsequent derivations. Considering

$$\mathbf{F}_\beta = \mathbf{F}_\beta(\{\mathbf{r}_\alpha\}) \quad \text{and} \quad \dot{\mathbf{F}}_\beta = \dot{\mathbf{F}}_\beta(\{\mathbf{r}_\alpha\}, \{\dot{\mathbf{r}}_\alpha\}), \tag{30}$$

we can have

$$\dot{\mathbf{F}}_\beta = \sum_\alpha \frac{\partial \mathbf{F}_\beta}{\partial \mathbf{r}_\alpha}\dot{\mathbf{r}}_\alpha, \tag{31}$$

which leads to the relation,

$$\frac{\partial \dot{\mathbf{F}}_\beta}{\partial \dot{\mathbf{r}}_\alpha} = \frac{\partial \mathbf{F}_\beta}{\partial \mathbf{r}_\alpha}. \tag{32}$$

Moreover

$$\ddot{\mathbf{F}}_\beta = \sum_\alpha \left(\frac{d}{dt}\left(\frac{\partial \mathbf{F}_\beta}{\partial \mathbf{r}_\alpha}\right)\dot{\mathbf{r}}_\alpha + \frac{\partial \mathbf{F}_\beta}{\partial \mathbf{r}_\alpha}\ddot{\mathbf{r}}_\alpha \right), \tag{33}$$

on the other hand,

$$\ddot{\mathbf{F}}_\beta = \sum_\alpha \left(\frac{\partial \dot{\mathbf{F}}_\beta}{\partial \mathbf{r}_\alpha}\dot{\mathbf{r}}_\alpha + \frac{\partial \dot{\mathbf{F}}_\beta}{\partial \dot{\mathbf{r}}_\alpha}\ddot{\mathbf{r}}_\alpha \right). \tag{34}$$

Comparing Eqs. (33) and (34) and utilizing (32), we obtain

$$\frac{d}{dt}\left(\frac{\partial \mathbf{F}_\beta}{\partial \mathbf{r}_\alpha}\right) = \frac{\partial \dot{\mathbf{F}}_\beta}{\partial \mathbf{r}_\alpha}. \tag{35}$$

Furthermore considering that,

$$\dot{\boldsymbol{\phi}}_\beta = \dot{\mathbf{F}}_\beta \boldsymbol{\chi}_\beta + \mathbf{F}_\beta \cdot \dot{\boldsymbol{\chi}}_\beta, \tag{36}$$

we can obtain,

$$\frac{\partial \dot{\boldsymbol{\phi}}_\beta}{\partial \dot{\mathbf{r}}_\alpha} = \frac{\partial \dot{\mathbf{F}}_\beta}{\partial \dot{\mathbf{r}}_\alpha}\boldsymbol{\chi}_\beta + \frac{\partial \mathbf{F}_\beta}{\partial \dot{\mathbf{r}}_\alpha}\dot{\boldsymbol{\chi}}_\beta = \frac{\partial \mathbf{F}_\beta}{\partial \mathbf{r}_\alpha}\boldsymbol{\chi}_\beta = \frac{\partial \boldsymbol{\phi}_\beta}{\partial \mathbf{r}_\alpha}. \tag{37}$$

Here, we assume that $\frac{\partial \mathbf{F}_\beta}{\partial \dot{\mathbf{r}}_\alpha} = 0$, according to Eq. (30).

By virtue of Eqs. (35)–(37), we have

$$\begin{aligned}\frac{\partial \dot{\boldsymbol{\phi}}_\beta}{\partial \mathbf{r}_\alpha} &= \frac{\partial \dot{\mathbf{F}}_\beta}{\partial \mathbf{r}_\alpha}\boldsymbol{\chi}_\beta + \frac{\partial \mathbf{F}_\beta}{\partial \mathbf{r}_\alpha}\dot{\boldsymbol{\chi}}_\beta = \frac{\partial \mathbf{F}_\beta}{\partial \mathbf{r}_\alpha}\dot{\boldsymbol{\chi}}_\beta + \frac{d}{dt}\left(\frac{\partial \mathbf{F}_\beta}{\partial \mathbf{r}_\alpha}\right)\boldsymbol{\chi}_\beta \\ &= \frac{d}{dt}\left(\frac{\partial \boldsymbol{\phi}_\beta}{\partial \mathbf{r}_\alpha}\right) = \frac{d}{dt}\left(\frac{\partial \dot{\boldsymbol{\phi}}_\beta}{\partial \dot{\mathbf{r}}_\alpha}\right).\end{aligned} \tag{38}$$

This relation is needed in the subsequent derivation. Considering the coarse scale Lagrange equation and utilizing the above relation, we have

$$\begin{aligned}\frac{d}{dt}\left(\frac{\partial \mathcal{L}_m}{\partial \dot{\mathbf{r}}_\alpha}\right) &= \frac{d}{dt}\left(M_\alpha \dot{\mathbf{r}}_\alpha + \sum_\beta \frac{\partial \mathcal{L}_m}{\partial \dot{\boldsymbol{\phi}}_\beta}\cdot\frac{\partial \dot{\boldsymbol{\phi}}_\beta}{\partial \dot{\mathbf{r}}_\alpha}\right) \\ &= M_\alpha \ddot{\mathbf{r}}_\alpha + \sum_\beta \frac{d}{dt}\left(\frac{\partial \mathcal{L}_m}{\partial \dot{\boldsymbol{\phi}}_\beta}\right)\cdot\frac{\partial \dot{\boldsymbol{\phi}}_\beta}{\partial \dot{\mathbf{r}}_\alpha} + \sum_\beta \frac{\partial \mathcal{L}_m}{\partial \dot{\boldsymbol{\phi}}_\beta}\cdot\frac{d}{dt}\left(\frac{\partial \dot{\boldsymbol{\phi}}_\beta}{\partial \dot{\mathbf{r}}_\alpha}\right) \\ &= M_\alpha \ddot{\mathbf{r}}_\alpha + \sum_\beta \frac{\partial \mathcal{L}_m}{\partial \boldsymbol{\phi}_\beta}\cdot\frac{\partial \boldsymbol{\phi}_\beta}{\partial \mathbf{r}_\alpha} + \sum_\beta \frac{\partial \mathcal{L}_m}{\partial \dot{\boldsymbol{\phi}}_\beta}\cdot\frac{d}{dt}\left(\frac{\partial \boldsymbol{\phi}_\beta}{\partial \mathbf{r}_\alpha}\right) \\ &= M_\alpha \ddot{\mathbf{r}}_\alpha + \sum_\beta \frac{\partial \mathcal{L}_m}{\partial \boldsymbol{\phi}_\beta}\cdot\frac{\partial \boldsymbol{\phi}_\beta}{\partial \mathbf{r}_\alpha} + \sum_\beta \frac{\partial \mathcal{L}_m}{\partial \dot{\boldsymbol{\phi}}_\beta}\cdot\frac{\partial \dot{\boldsymbol{\phi}}_\beta}{\partial \mathbf{r}_\alpha}.\end{aligned} \tag{39}$$

Furthermore,

$$\frac{\partial \mathcal{L}_m}{\partial \mathbf{r}_\alpha} = \sum_{\beta\neq\alpha}\sum_{i\in\alpha,\, j\in\beta} V'(r_{ij})\frac{\mathbf{r}_{ij}}{|\mathbf{r}_{ij}|} - \sum_{i\in\alpha}\mathbf{b}_i + \sum_\beta \frac{\partial \mathcal{L}_m}{\partial \boldsymbol{\phi}_\beta}\cdot\frac{\partial \boldsymbol{\phi}_\beta}{\partial \mathbf{r}_\alpha} + \sum_\beta \frac{\partial \mathcal{L}_m}{\partial \dot{\boldsymbol{\phi}}_\beta}\cdot\frac{\partial \dot{\boldsymbol{\phi}}_\beta}{\partial \mathbf{r}_\alpha}. \tag{40}$$

Substituting expressions (39) and (40) into the coarse scale Lagrange equation, we have

$$\frac{d}{dt}\left(\frac{\partial \mathcal{L}_m}{\partial \dot{\mathbf{r}}_\alpha}\right) - \frac{\partial \mathcal{L}_m}{\partial \mathbf{r}_\alpha} = 0 \;\rightarrow\; M_\alpha \ddot{\mathbf{r}}_\alpha = \sum_{\beta\neq\alpha}\sum_{i\in\alpha,\, j\in\beta} V'(r_{ij})\frac{\mathbf{r}_{ij}}{|\mathbf{r}_{ij}|} + \mathcal{B}_\alpha \tag{41}$$

where $\mathcal{B}_\alpha = \sum_i \mathbf{b}_i$. Note that $-V'(r_{ij})\frac{\mathbf{r}_{ij}}{|\mathbf{r}_{ij}|} = \mathbf{f}_{ij}$ is the pair force between atoms i and j. If one would like to include the macroscale traction boundary condition as indicated in Fig. 1, one needs to add another term on the center of mass of the boundary cells. In this case, we can redefine the external force density as follows (see [36]),

$$\mathcal{B}_\alpha = S_\alpha \bar{\mathbf{t}}_\alpha + \Omega_\alpha \bar{\mathbf{b}}_\alpha, \tag{42}$$

where S_α is the area of macroscale traction boundary of αth cell, $\bar{\mathbf{t}}_\alpha$ is the traction vector on S_α; and $\bar{\mathbf{b}}_\alpha = \sum_i \mathbf{b}_i/\Omega_\alpha$.

Then we can rewrite the above equation as,

$$M_\alpha \ddot{\mathbf{r}}_\alpha = -\sum_{\beta\neq\alpha}\sum_{i\in\alpha,\, j\in\beta} \mathbf{f}_{ij} + \mathcal{B}_\alpha. \tag{43}$$

The first term in the right hand side (RHS) of Eq. (43) represents the cell-to-cell interactions. We can also rewrite the first term of RHS of Eq. (43) as

$$\sum_{\beta\neq\alpha}\sum_{i\in\alpha,\, j\in\beta} \mathbf{f}_{ij} = \sum_{\beta\neq\alpha} \mathbf{f}_{\alpha\beta}, \quad \text{where } \mathbf{f}_{\alpha\beta} := \sum_{i\in\alpha}\sum_{j\in\beta} \mathbf{f}_{ij}. \tag{44}$$

Then Eq. (43) can be written in terms of coarse grain variables completely,

$$M_\alpha \ddot{\mathbf{r}}_\alpha = -\sum_{\beta\neq\alpha} \mathbf{f}_{\alpha\beta} + \mathcal{B}_\alpha. \tag{45}$$

where the Greek letters α, β denote the centers of mass of MD cells.

In Eq. (44), the cell-to-cell interaction term consists of all the atomic bond forces that passing through the surface of the cell, which is actually the non-local divergence of the Cauchy stress ($\nabla \cdot \boldsymbol{\sigma}_\alpha$) generated by the atomic interaction from outside the cell multiply the volume Ω_α. This can be seen as follows,

$$-\sum_{\beta\neq\alpha}\sum_{i\in\alpha, j\in\beta} \mathbf{f}_{ij} \approx \int_{\partial\Omega_\alpha} \boldsymbol{\sigma}\cdot\mathbf{n}dS = \int_{\Omega_\alpha} \nabla\cdot\boldsymbol{\sigma} dV \approx \nabla\cdot\boldsymbol{\sigma}_\alpha \Omega_\alpha.$$

Thus Eq. (43) may be interpreted as,

$$M_\alpha \ddot{\mathbf{r}}_\alpha = (\nabla \cdot \boldsymbol{\sigma}_\alpha)\Omega_\alpha + \mathcal{B}_\alpha \tag{46}$$

which is a coarse-grain version of the Balance of Linear Momentum. Eq. (46) not only establishes a link from molecular dynamics to continuum mechanics, but also provides an alternative computational formulation, which is explained as follows.

First we can rewrite the divergence of the Cauchy stress as

$$\begin{aligned}\Omega_\alpha \nabla_r \cdot \boldsymbol{\sigma}_\alpha &= \tilde{\Omega}_\alpha J \nabla_{\mathcal{R}} \cdot \boldsymbol{\sigma}_\alpha \left(\frac{\partial \boldsymbol{\mathcal{R}}}{\partial \mathbf{r}}\right) = \tilde{\Omega}_\alpha \left(\nabla_{\mathcal{R}} \cdot \left(J\boldsymbol{\sigma}_\alpha \mathbf{F}_\alpha^{-T}\right) - \boldsymbol{\sigma}_\alpha \cdot \nabla_{\mathcal{R}} \cdot (J\mathbf{F}_\alpha^{-T})\right) \\ &= \tilde{\Omega}_\alpha \nabla_{\mathcal{R}} \cdot \left(J\boldsymbol{\sigma}_\alpha \mathbf{F}_\alpha^{-T}\right) = \tilde{\Omega}_\alpha \nabla_{\mathcal{R}} \cdot \boldsymbol{\mathcal{P}}_\alpha,\end{aligned}$$

where $\tilde{\Omega}_\alpha$ is the volume of the MD cell in the intermediate configuration, i.e. $\boldsymbol{\mathcal{R}}$-configuration, and $J := det(\mathbf{F}_\alpha) = \Omega_\alpha/\tilde{\Omega}_\alpha$. In the above derivation, the Piola identity $\nabla_{\mathcal{R}} \cdot (J\mathbf{F}^{-T}) = 0$ is used, and moreover $\boldsymbol{\mathcal{P}}_\alpha = J\boldsymbol{\sigma}_\alpha \mathbf{F}_\alpha^{-T}$ is the first Piola–Kirchhoff stress with respect to the current configuration ($\mathbf{r}$-configuration) and the referential configuration ($\boldsymbol{\mathcal{R}}$-configuration), which can be shown as

$$\boldsymbol{\mathcal{P}}_\alpha = \boldsymbol{\mathcal{P}}_\alpha^{Viral} = \frac{1}{\tilde{\Omega}_\alpha}\sum_{i\in\alpha}\left(-\boldsymbol{\phi}_\alpha m_i \dot{\mathbf{S}}_i \otimes \dot{\mathbf{S}}_i + \frac{1}{2}\sum_{j\in\alpha, j\neq i} \mathbf{f}_{ij}\otimes\mathbf{S}_{ij}\right)\cdot\boldsymbol{\chi}_\alpha^T, \tag{47}$$

when the equilibrium state is reached at the mesoscale. The detailed derivation of Eq. (47) will be discussed in the subsequent sections, and our purpose here is to derive the macroscale dynamic equation.

Now Eq. (46) can be re-written as

$$M_\alpha \ddot{\mathbf{r}}_\alpha = \tilde{\Omega}_\alpha \nabla_{\mathcal{R}} \cdot \boldsymbol{\mathcal{P}}_\alpha + \mathcal{B}_\alpha. \tag{48}$$

Recall that the coarse scale deformation gradient may be approximated as (9),

$$\mathbf{F}_\alpha = \nabla_{\mathcal{R}} \otimes \mathbf{r}_\alpha \approx \left(\sum_{\beta=1}^{N_h} \omega(|\mathbf{R}_{\alpha\beta}|)\mathbf{r}_{\alpha\beta}\otimes\mathbf{R}_{\alpha\beta}\tilde{\Omega}_\beta\right)\cdot\mathbf{M}_\alpha^{-1}, \tag{49}$$

which indicates that the structure of the discrete differential operator may be expressed as,

$$\nabla_{\mathcal{R}} \otimes \left(\mathbf{f}_\alpha\right) \approx \left(\sum_{\beta=1}^{N_h} \omega(|\mathbf{R}_{\alpha\beta}|)(\mathbf{f}_\beta - \mathbf{f}_\alpha)\otimes\mathbf{R}_{\alpha\beta}\tilde{\Omega}_\beta\right)\cdot\mathbf{M}_\alpha^{-1}.$$

Following the same procedure, we can define the discrete gradient operator as,

$$\nabla_{\mathcal{R}} \cdot \left(\mathbf{f}_\alpha\right) \approx \left(\sum_{\beta=1}^{N_h} \omega(|\mathbf{R}_{\alpha\beta}|)(\mathbf{f}_\beta - \mathbf{f}_\alpha)\cdot\mathbf{R}_{\alpha\beta}\tilde{\Omega}_\beta\right)\cdot\mathbf{M}_\alpha^{-1}. \tag{50}$$

Note that the center of mass positions, $\mathbf{R}_\alpha$ or $\mathbf{R}_\beta$, are the same in the intermediate configuration ($\boldsymbol{\mathcal{R}}$) as that in the referential configuration ($\mathbf{R}$).

Finally, we can approximate Eq. (48) as

$$M_\alpha \ddot{\mathbf{r}}_\alpha \approx \left(\sum_{\beta=1}^{N_h} \omega(|\mathbf{R}_{\alpha\beta}|)(\boldsymbol{\mathcal{P}}_\beta - \boldsymbol{\mathcal{P}}_\alpha) \cdot \mathbf{R}_{\alpha\beta} \tilde{\Omega}_\beta \right) \cdot \mathbf{M}_\alpha^{-1} + \mathcal{B}_\alpha. \tag{51}$$

This is an alternative computation formulation in comparison to Eq. (43), because one does not need to calculate interactions among different cells but only calculate the Virial stress in each cell. This formulation provides a natural passage between molecular dynamics and continuum mechanics coupling.

3.2. Mesoscale dynamic equations

We now exam the mesoscale Lagrange equation. Considering the derivative terms with respect to the chosen mesoscale variable, i.e. $\dot{\boldsymbol{\phi}}_\alpha$ and $\boldsymbol{\phi}_\alpha$, we first have,

$$\frac{\partial \mathcal{L}_m}{\partial \dot{\boldsymbol{\phi}}_\alpha} = \dot{\boldsymbol{\phi}}_\alpha \cdot \mathbf{J}_\alpha^S \;\rightarrow\; \frac{d}{dt}\left(\frac{\partial \mathcal{L}_m}{\partial \dot{\boldsymbol{\phi}}_\alpha} \right) = \frac{d}{dt}(\dot{\boldsymbol{\phi}}_\alpha \cdot \mathbf{J}_\alpha^S) = \ddot{\boldsymbol{\phi}}_\alpha \cdot \mathbf{J}_\alpha^S, \tag{52}$$

and then we have,

$$\begin{aligned} \frac{\partial \mathcal{L}_m}{\partial \boldsymbol{\phi}_\alpha} &= \frac{1}{2} \sum_i m_i \dot{\mathbf{S}}_i \frac{\partial \mathbf{C}_\alpha}{\partial \boldsymbol{\phi}_\alpha} \dot{\mathbf{S}}_i - \frac{1}{2} \sum_{i,j \in \alpha} V'(r_{ij}) \frac{\mathbf{r}_{ij}}{|\mathbf{r}_{ij}|} \cdot \frac{\partial \mathbf{r}_{ij}}{\partial \boldsymbol{\phi}_\alpha} \\ &\quad - \sum_\beta \sum_{\substack{i \in \alpha \\ j \in \beta \neq \alpha}} V'(r_{ij}) \frac{\mathbf{r}_{ij}}{|\mathbf{r}_{ij}|} \cdot \frac{\partial \mathbf{r}_{ij}}{\partial \boldsymbol{\phi}_\alpha} - \sum_{i \in \alpha} \mathbf{b}_i \cdot \frac{\partial \mathbf{r}_i}{\partial \boldsymbol{\phi}_\alpha} \\ &= \boldsymbol{\phi}_\alpha \sum_i m_i \dot{\mathbf{S}}_i \otimes \dot{\mathbf{S}}_i - \frac{1}{2} \sum_{i,j \in \alpha} \mathbf{f}_{ij} \otimes \mathbf{S}_{ij} + \sum_\beta \sum_{\substack{i \in \alpha \\ j \in \beta \neq \alpha}} \mathbf{f}_{ij} \otimes \mathbf{S}_i + \sum_{i \in \alpha} \mathbf{b}_i \otimes \mathbf{S}_i. \end{aligned} \tag{53}$$

Finally, the mesoscale Lagrange equations have the form,

$$\ddot{\boldsymbol{\phi}}_\alpha \cdot \mathbf{J}_\alpha^S = \boldsymbol{\phi}_\alpha \sum_i m_i \dot{\mathbf{S}}_i \otimes \dot{\mathbf{S}}_i - \frac{1}{2} \sum_{i,j \in \alpha} \mathbf{f}_{ij} \otimes \mathbf{S}_{ij} + \sum_\beta \sum_{\substack{i \in \alpha \\ j \in \beta \neq \alpha}} \mathbf{f}_{ij} \otimes \mathbf{S}_{ij} + \sum_{i \in \alpha} \mathbf{b}_i \otimes \mathbf{S}_i. \tag{54}$$

To understand physical meanings of the above equation, we can define the mesoscale 1st Piola–Kirchhoff stress tensors as,

$$\mathbf{P}_\alpha^{Virial} := \sum_{i \in \alpha} \left(-\boldsymbol{\phi}_\alpha m_i \dot{\mathbf{S}}_i \otimes \dot{\mathbf{S}}_i + \frac{1}{2} \sum_{j \in \alpha, j \neq i} \mathbf{f}_{ij} \otimes \mathbf{S}_{ij} \right) \tag{55}$$

$$\mathbf{P}_\alpha^{ext} = \sum_{\beta \neq \alpha} \sum_{i \in \alpha, j \in \beta} \mathbf{f}_{ij} \otimes \mathbf{S}_{ij} = \boldsymbol{\phi}_\alpha \cdot \left(\sum_{\beta \neq \alpha} \sum_{i \in \alpha, j \in \beta} V'(r_{ij}) \frac{\mathbf{S}_{ij} \otimes \mathbf{S}_{ij}}{r_{ij}} \right), \tag{56}$$

where $\mathbf{P}_\alpha^{Virial}$ and $\mathbf{P}_\alpha^{ext}$ are the first Piola–Kirchhoff stress of the αth cell, which are the two-point tensors defined on the current configuration i.e $\mathbf{r}$-configuration and the statistical configuration, i.e. $\mathbf{S}$-configuration.

Figuratively speaking, these tensors have two legs, one is in $\mathbf{r}$-configuration and the other is in $\mathbf{S}$-configuration. If we push the leg in $\mathbf{S}$-configuration forward to the intermediate configuration $\boldsymbol{\mathcal{R}}$-configuration, i.e. $\boldsymbol{\mathcal{R}}_i = \boldsymbol{\chi} \cdot \mathbf{S}_i$, the corresponding first Piola–Kirchhoff stress will have the following expression,

$$\boldsymbol{\mathcal{P}}_\alpha^{Virial} = \frac{1}{\tilde{\Omega}_\alpha} \sum_{i \in \alpha} \left(-\boldsymbol{\phi}_\alpha m_i \dot{\mathbf{S}}_i \otimes \dot{\mathbf{S}}_i + \frac{1}{2} \sum_{j \in \alpha, j \neq i} \mathbf{f}_{ij} \otimes \mathbf{S}_{ij} \right) \cdot \boldsymbol{\chi}_\alpha^T, \tag{57}$$

which is used in Eq. (47).

Remark 3.1. 1. There is no 1/2 factor in Eq. (56). This is because $i \in \alpha$ but $j \in \beta$, and $\alpha \neq \beta$;
2. If we define,

$$\boldsymbol{\sigma}_{\alpha}^{ext} = \frac{1}{\Omega_\alpha}\sum_i \sum_{j\neq i} V'(r_{ij})\left(\frac{\mathbf{r}_{ij}\otimes \mathbf{r}_{ij}}{r_{ij}}\right) = \boldsymbol{\phi}_\alpha \cdot \left(\frac{1}{\Omega_\alpha}\sum_i \sum_{j\neq i} V'(r_{ij})\left(\frac{\mathbf{S}_{ij}\otimes \mathbf{S}_{ij}}{r_{ij}}\right)\right)\cdot \boldsymbol{\phi}_\alpha^T, \tag{58}$$

where Ω_α is the volume of the αth cell in spatial configuration, i.e. $\mathcal{B}_c$-configuration, $\mathbf{P}_\alpha^{ext}$ can then be expressed by the external Cauchy stress as

$$\mathbf{P}_\alpha^{ext} = det(\boldsymbol{\phi}_\alpha)\boldsymbol{\sigma}_\alpha^{ext}\cdot \boldsymbol{\phi}_\alpha^{-T}. \tag{59}$$

3. The Jacobian of the micromorphic gradient is

$$det(\boldsymbol{\phi}_\alpha) = det(\boldsymbol{\chi}_\alpha)det(\mathbf{F}_\alpha) = \frac{\tilde{\Omega}_\alpha}{\Omega_{\alpha 0}}\frac{\Omega_\alpha}{\tilde{\Omega}_\alpha} = \frac{\Omega_\alpha}{\Omega_{\alpha 0}} \tag{60}$$

where $\Omega_{\alpha 0}$ is the volume of the initial MD cell.

With above definitions of stresses, we can recast the mesoscale dynamics equations as

$$\ddot{\boldsymbol{\phi}}_\alpha \cdot \mathbf{J}_\alpha^S = -\left(\mathbf{P}_\alpha^{Virial} - \mathbf{P}_\alpha^{ext}\right) + \mathbf{M}_\alpha \tag{61}$$

where $\mathbf{P}_\alpha^{Virial}$ is given by Eq. (55), and $\mathbf{P}_\alpha^{ext}$ is given by Eq. (56) or (59), $\mathbf{M}_\alpha = \sum_{i\in\alpha}\mathbf{b}_i \otimes \mathbf{S}_i$ is the mesoscale external couple. Note that Eqs. (55) and (56) are insightful, because they resolve one of outstanding debates on the definition of the Virial stress. Eq. (55) is basically the mathematical definition of the Virial stress e.g. [44,45]. However, Zhou [46] argued that the kinetic energy part should be dropped out in the stress calculation, even though many disagreed, e.g. [47,48]. We now see from Eqs. (55) and (56) that if the stress is internally generated, the definition of the Virial stress is the original form of the Virial stress; but if the stress is an external stress, then the kinetic energy part should drop out from its expression. This is because that the current formulation of the multiscale micromorphic molecular dynamics is an adiabatic formulation, which does not consider the heat exchange among the cells. If in Eq. (61), $\ddot{\boldsymbol{\phi}}_\alpha = 0$, we have $\mathbf{P}_\alpha^{ext} = \mathbf{P}_\alpha^{Virial} \rightarrow \mathcal{P}_\alpha^{ext} = \mathcal{P}_\alpha^{Virial}$, which is the proof of Eq. (47).

3.3. Microscale dynamic equations

After evaluating the fine scale Lagrange equation for $i \in \alpha$, we first have

$$\frac{d}{dt}\frac{\partial \mathcal{L}_m}{\partial \dot{\mathbf{S}}_i} = m_i\left(\mathbf{C}_\alpha \ddot{\mathbf{S}}_i + \dot{\mathbf{C}}_\alpha \cdot \dot{\mathbf{S}}_i\right). \tag{62}$$

The derivative of fine scale Lagrange equation with respect to $\mathbf{S}_i$ has two cases,

$$\text{(a) } \alpha = \beta: \quad \frac{\partial \mathcal{L}_m}{\partial \mathbf{S}_i} = -\frac{1}{2}\sum_{j\neq i}\left(\frac{V'(r_{ij})}{r_{ij}}\mathbf{C}_\alpha \cdot \mathbf{S}_{ij}\right) \tag{63}$$

$$\text{(b) } \alpha \neq \beta: \quad \frac{\partial \mathcal{L}_m}{\partial \mathbf{S}_i} = -\frac{1}{2}\sum_{\alpha\neq\beta}\sum_{j\neq i}\left(\frac{V'(r_{ij})}{r_{ij}}\boldsymbol{\phi}_\alpha^T \cdot \mathbf{r}_{ij}\right), \tag{64}$$

where $\mathbf{r}_{ij} = \mathbf{r}_{\alpha\beta} + \boldsymbol{\phi}_\beta \cdot \mathbf{S}_j - \boldsymbol{\phi}_\alpha \cdot \mathbf{S}_i$. This is because,

$$\frac{\partial V}{\partial \mathbf{S}_i} = \frac{\partial V}{\partial r_{ij}}\frac{\partial r_{ij}}{\partial \mathbf{r}_{ij}}\frac{\partial \mathbf{r}_{ij}}{\partial \mathbf{S}_i} = V'(r_{ij})\frac{\mathbf{r}_{ij}}{r_{ij}}\cdot \Phi_\alpha = \frac{V'(r_{ij})}{r_{ij}}\Phi_\alpha^T \cdot \mathbf{r}_{ij},$$

and $\mathbf{r}_{ij} = \Phi_\alpha \cdot \mathbf{S}_{ij}$ only when $\alpha = \beta$.

Combining these two equations i.e. Eqs. (63) and (64) as well as Eq. (62), we finally have

$$m_i\ddot{\mathbf{S}}_i + \frac{1}{2}\boldsymbol{\phi}_\alpha^{-1}\sum_\beta\sum_{i\neq j}\left(\frac{V'(r_{ij})}{r_{ij}}(\mathbf{r}_{\alpha\beta} + \boldsymbol{\phi}_\beta\cdot\mathbf{S}_j - \boldsymbol{\phi}_\alpha\cdot\mathbf{S}_i)\right) + m_i\mathbf{C}_\alpha^{-1}\dot{\mathbf{C}}_\alpha\cdot\dot{\mathbf{S}}_i + \boldsymbol{\phi}_\alpha^{-1}\cdot\mathbf{b}_i = \mathbf{0}, \tag{65}$$

where $i \in \alpha$. One may note that the second term in Eq. (65) contains both interaction of atoms within the αth cell and between two different cells, i.e. the case $i \in \alpha,\ j \in \beta$ and $\beta \neq \alpha$.

In summary, the three scale governing equations of Multiscale Micromorphic Molecular Dynamics are as follows,

$$M_\alpha \ddot{\mathbf{r}}_\alpha = -\sum_{\beta\neq\alpha}\sum_{i\in\alpha,\, j\in\beta} \mathbf{f}_{ij} + S_\alpha \bar{\mathbf{t}}_\alpha + \Omega_\alpha \bar{\mathbf{b}}_\alpha, \tag{66}$$

$$\ddot{\boldsymbol{\phi}}_\alpha \cdot \mathbf{J}^S_\alpha = -(\mathbf{P}^{Virial}_\alpha - \mathbf{P}^{ext}_\alpha) + \mathbf{M}_\alpha, \tag{67}$$

$$m_i \ddot{\mathbf{S}}_i = -m_i \mathbf{C}^{-1}_\alpha \cdot \dot{\mathbf{C}}_\alpha \cdot \dot{\mathbf{S}}_i + \boldsymbol{\phi}^{-1}_\alpha \left(\sum_\beta \sum_{j\in\beta\neq i\in\alpha} \mathbf{f}_{ji} + \mathbf{b}_i \right), \tag{68}$$

where the micromorphic deformation tensor is $\boldsymbol{\phi}_\alpha = \mathbf{F}_\alpha \cdot \boldsymbol{\chi}_\alpha$. One can see from Eq. (66) that the macroscale traction boundary condition is embedded in the coarse scale dynamic equation.

4. Computational algorithms

Suppose that the αth cell has N_α atoms, and the total degrees of freedom of the atomistic system will be $3N_\alpha$. On the other hand, Eqs. (66)–(68) have $3 + 9 + 3N_\alpha$ degrees of freedom. Since MMMD is only a re-partition of original first principle MD, it should have the same degrees of freedom as the original MD, i.e. $3N_\alpha$. Therefore, the MMMD dynamic system (66)–(68) is an overdetermined system. We need additional 12 constraints to guarantee the multiscale system equivalent to the original first-principle molecular dynamics system. The twelve constraints that we impose to the multiscale system are:

$$(I). \quad \sum_i m_i \mathbf{S}_i = \mathbf{0}, \tag{69}$$

which stems from Eq. (3), and it ensures that $\mathbf{S}_i$ have zero mean. Even though at the beginning of the computation, Eq. (69) satisfies; during the computation, it will be gradually violated.

Similarly, at the beginning of the simulation, $\|\mathbf{S}_i\| \leq 1$. However, after a while, the inequality starts to fail. Hence, the second constraint is the following **renormalization** condition,

$$(II). \quad \boldsymbol{\chi}_\alpha \cdot \mathbf{S}_i = \underbrace{\boldsymbol{\chi} \cdot \mathbf{h}}_{\tilde{\boldsymbol{\chi}}_\alpha} \cdot \underbrace{\mathbf{h}^{-1} \cdot \mathbf{S}_i}_{\tilde{\mathbf{S}}_i} = \tilde{\boldsymbol{\chi}}_\alpha \cdot \tilde{\mathbf{S}}_i, \tag{70}$$

which ensures the new scaled atomistic position vector $\tilde{\mathbf{S}}_i := \mathbf{h}^{-1}\mathbf{S}_i \ \rightarrow\ \|\tilde{\mathbf{S}}_i\| < 1$. To do so, we can construct an envelop shape tensor $\mathbf{h} = [\mathbf{S}_I, \mathbf{S}_{II}, \mathbf{S}_{III}]$ such that

$$S_{I1} = \max\{|S_{i1}|\}_{i=1}^{N_\alpha}, \qquad S_{I2} = \max\{|S_{i2}|\}_{i=1}^{N_\alpha}, \quad \text{and} \quad S_{III3} = \max\{|S_{i3}|\}_{i=1}^{N_\alpha}, \tag{71}$$

with $\mathbf{S}_I$, $\mathbf{S}_{II}$ and $\mathbf{S}_{III}$ not being coplanar. If $\mathbf{h}$ can be selected, we can renormalize $\mathbf{S}_i$, as graphically demonstrated in Fig. 4. It should be noted that the selection or construction of $\mathbf{h}$, i.e. Eq. (71), is not always possible for a given molecular dynamics system. However, if $\mathbf{J}^S_\alpha(t)$ is a spherical tensor, the construction of $\mathbf{h}$ is not only possible, but trivial in computation (see Fig. 5).

If this process is slow, we may assume that $\dot{\mathbf{h}} \approx 0$. Hence the kinematic energy of MMMD is invariant under the renormalization, which is also called as the modular transformation if $\mathbf{h} = \mathbf{R} \in SO(3)$ (see [49]). Based on the above arguments, computationally, we can use the Lagrangian multiplier method to enforce the zero-mean condition, and two statistical conditions. We first define the three constraint functions,

$$\mathbf{G}_1 := \sum_i m_i \mathbf{S}_i; \qquad \mathbf{G}_2 := \mathbf{J}^S_\alpha(t) - \mathbf{J}^S_\alpha(0), \quad \text{and} \quad \mathbf{G}_3 := \mathrm{diag}(\mathbf{J}^S_\alpha(t)) - \mathrm{Tr}(\mathbf{J}^S_\alpha(0))\mathrm{diag}(\mathbf{I}^{(2)}). \tag{72}$$

These constraints can be enforced by the Lagrangian multiplier method,

$$\mathcal{L}^*_\alpha = \mathcal{L}_\alpha - \boldsymbol{\lambda}_{\alpha 1} \cdot \mathbf{G}_{\alpha 1} - \boldsymbol{\lambda}_{\alpha 2} : \mathbf{G}_{\alpha 2} - \boldsymbol{\lambda}_{\alpha 3} \cdot \mathbf{G}_{\alpha 3} \quad \text{and} \quad \mathcal{L}^*_m = \sum_\alpha \mathcal{L}^*_\alpha, \tag{73}$$

where $\boldsymbol{\lambda}_{\alpha 1}$ and $\boldsymbol{\lambda}_{\alpha 3}$ are vector multipliers, and $\boldsymbol{\lambda}_{\alpha 2}$ is a tensorial multiplier.

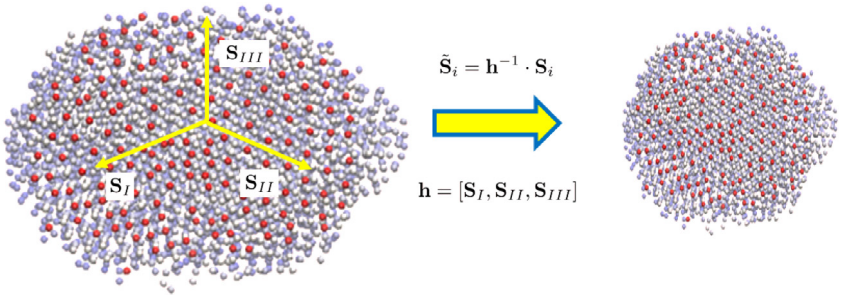

Fig. 5. Illustration of renormalization of the statistical configuration.

Remark 4.1. 1. Eq. (69) provides 3 constraints, and Eq. (71) provides 9 constraints, while Eq. (73) also provides $3 + 6 + 3 = 12$ constraints, because $\mathbf{G}_2$ is a symmetric tensor. Moreover, the above renormalization algorithm may break down if there is long range atom diffusion, or a strong stochastic random motion, so that the local equilibrium assumption is no longer valid. This may be the case for materials in fluid state, or liquid phase. Therefore, the proposed multiscale molecular dynamics is only suitable for solid materials.

2. The original PR-MD is conceptually employed the following Lagrangian,

$$\mathcal{L}^*_{PR} = \mathcal{L}_{PR} - \lambda\Big(\text{Trace}(\mathbf{J}^S_\alpha) - W_\alpha\Big).$$

The augmented Lagrangian equations resulted from Eq. (73) can be solved by using the well-known SHAKE or RATTLE algorithms e.g. [50–52]. In the following, we outline the basic steps for solving the fine scale equation of motion due to the augmented Lagrangian (73). If we omit the constraint $\mathbf{G}_{\alpha 3}$ and the body force at atomistic resolution, we have

$$\frac{d}{dt}\frac{\partial \mathcal{L}^*_m}{\partial \dot{\mathbf{S}}_i} - \frac{\partial \mathcal{L}^*_m}{\partial \mathbf{S}_i} = 0 \;\rightarrow$$

$$\ddot{\mathbf{S}}_i = -\mathbf{C}^{-1}_\alpha \cdot \dot{\mathbf{C}}_\alpha \cdot \dot{\mathbf{S}} + \boldsymbol{\phi}^{-1}_\alpha \sum_\beta \sum_{\alpha_i \neq \beta_j} \frac{1}{m_i}\mathbf{f}_{ji} - \mathbf{C}^{-1}_\alpha \cdot \boldsymbol{\lambda}_{\alpha 1} - \mathbf{C}^{-1}_\alpha \cdot \boldsymbol{\lambda}_{\alpha 2} \cdot \mathbf{S}_i \tag{74}$$

where α_i denote the ith atom in the αth cell, and β_j denotes the jth atom in the βth cell; and free index β can run through the fixed index α.

For simplicity, we let $\mathbf{F}_i := -m_i\mathbf{C}^{-1}_\alpha \cdot \dot{\mathbf{C}}_\alpha \cdot \dot{\mathbf{S}}_i + \boldsymbol{\phi}^{-1}_\alpha \sum_\beta \sum_{\alpha_i \neq \beta_j} \mathbf{f}_{ji}$. Then we can use an original Verlet based predictor–corrector algorithm [53] combining with operator splitting algorithm to integrate Eq. (74),

$$\mathbf{S}^{(p1)}_i(t + \Delta t) = 2\mathbf{S}_i(t) - \mathbf{S}_i(t - \Delta t) + \frac{\Delta t^2}{m_i}\mathbf{F}^{(p)}_i \tag{75}$$

$$\mathbf{S}^{(p2)}_i(t + \Delta t) = \mathbf{S}^{(p1)}_i(t + \Delta t) - \Delta t^2\mathbf{C}^{-1}_\alpha(t) \cdot \boldsymbol{\lambda}^{(p)}_{\alpha 1}(\Delta t) \tag{76}$$

$$\mathbf{S}^{(p3)}_i(t + \Delta t) = \mathbf{S}^{(p2)}_i(t + \Delta t) - \Delta t^2\mathbf{C}^{-1}_\alpha(t) \cdot \boldsymbol{\lambda}^{(p)}_{\alpha 2}(\Delta t) \cdot \mathbf{S}^{(p2)}_i(t + \Delta t). \tag{77}$$

where the superscript "p" means predict phase, and the predicted velocity value is

$$\dot{\mathbf{S}}^{(p)}_i = \frac{\mathbf{S}_i(t) - \mathbf{S}_i(t - \Delta t)}{\Delta t} \;\rightarrow\; \mathbf{F}^{(p)}_i := -m_i\mathbf{C}^{-1}_\alpha \cdot \dot{\mathbf{C}}_\alpha \cdot \dot{\mathbf{S}}^{(p)}_i + \boldsymbol{\phi}^{-1}_\alpha \sum_\beta \sum_{\alpha_i \neq \beta_j} \mathbf{f}_{ji}(\mathbf{S}_i).$$

Imposing the first constraint condition, we obtain

$$\sum_i m_i\mathbf{S}^{(p2)}_i = \mathbf{0} \;\rightarrow\; \boldsymbol{\lambda}^{(p)}_{\alpha 1} = \mathbf{C}_\alpha(t) \cdot \left(\frac{\sum_i m_i\mathbf{S}^{(p1)}_i(t + \Delta t)}{(\Delta t)^2\Big(\sum_i m_i\Big)}\right). \tag{78}$$

Imposing the second constraint condition $\sum_i m_i \mathbf{S}_i^{(p3)} \otimes \mathbf{S}_i^{(p3)} = \mathbf{J}_\alpha^S(0)$ and assuming $\boldsymbol{\lambda}_{\alpha 2}$ is symmetric, we have

$$\sum_i m_i \mathbf{S}_i^{(p2)} \otimes \mathbf{S}_i^{(p2)} - 2(\Delta t)^2 \mathbf{C}_\alpha^{-1} \boldsymbol{\lambda}_{\alpha 2}^{(p)} \sum_i m_i \mathbf{S}_i^{(p2)} \otimes \mathbf{S}_i^{(p2)} + (\Delta t)^4 \sum_i m_i (\mathbf{C}_\alpha^{-1} \cdot \boldsymbol{\lambda}_2 \cdot \mathbf{S}_i^{(p2)}) \otimes (\mathbf{C}_\alpha^{-1} \cdot \boldsymbol{\lambda}_2^{(p)} \cdot \mathbf{S}_i^{(p2)}) = \mathbf{J}_\alpha^S(0). \tag{79}$$

Neglecting the higher order terms, we finally obtain

$$\boldsymbol{\lambda}_{\alpha 2}^{(p)} = \frac{1}{2(\Delta t)^2} \mathbf{C}_\alpha \left\{ \sum_i m_i \mathbf{S}_i^{(p2)} \otimes \mathbf{S}_i^{(p2)} - \mathbf{J}_\alpha^S(0) \right\} \left(\sum_i m_i \mathbf{S}_i^{(p2)} \otimes \mathbf{S}_i^{(p2)} \right)^{-1}. \tag{80}$$

Substituting (78) and (80) into (76) and (77), we finish the predictor phase. Repeating the same procedure in the following corrector phase, we have

$$\mathbf{S}_i^{(c1)}(t + \Delta t) = 2\mathbf{S}_i(t) - \mathbf{S}_i(t - \Delta t) + \frac{\Delta t^2}{2m_i} \left(\mathbf{F}_i^{(c)} + \mathbf{F}_i^{(p)} \right) \tag{81}$$

$$\mathbf{S}_i^{(c2)}(t + \Delta t) = \mathbf{S}_i^{(c1)}(t + \Delta t) - \Delta t^2 \mathbf{C}_\alpha^{-1}(t) \cdot \boldsymbol{\lambda}_{\alpha 1}^{(c)}(\Delta t) \tag{82}$$

$$\mathbf{S}_i^{(c3)}(t + \Delta t) = \mathbf{S}_i^{(c2)}(t + \Delta t) - \Delta t^2 \mathbf{C}_\alpha^{-1}(t) \cdot \boldsymbol{\lambda}_{\alpha 2}^{(c)}(\Delta t) \cdot \mathbf{S}_i^{(c2)}(t + \Delta t), \tag{83}$$

where the superscript "c" means the corrector phase, and the predicted velocity value is

$$\dot{\mathbf{S}}_i^{(c)} = \frac{\mathbf{S}_i^{(p3)}(t + \Delta t) - \mathbf{S}_i(t)}{\Delta t} \rightarrow \mathbf{F}_i^{(c)} := -m_i \mathbf{C}_\alpha^{-1} \cdot \dot{\mathbf{C}}_\alpha \cdot \dot{\mathbf{S}}_i^{(c)} + \boldsymbol{\phi}_\alpha^{-1} \sum_\beta \sum_{\alpha_i \neq \beta_j} \mathbf{f}_{ji}(\mathbf{S}_i^{(p3)}),$$

with the correction Lagrangian multipliers expressed as

$$\boldsymbol{\lambda}_{\alpha 1}^{(c)} = \mathbf{C}_\alpha(t) \cdot \left(\frac{\sum_i m_i \mathbf{S}_i^{(c1)}}{(\Delta t)^2 \left(\sum_i m_i \right)} \right), \quad \text{and} \tag{84}$$

$$\boldsymbol{\lambda}_{\alpha 2}^{(c)} = \frac{1}{2(\Delta t)^2} \mathbf{C}_\alpha(t) \left\{ \sum_i m_i \mathbf{S}_i^{(c2)} \otimes \mathbf{S}_i^{(c2)} - \mathbf{J}_\alpha^S(0) \right\} \left(\sum_i m_i \mathbf{S}_i^{(c2)} \otimes \mathbf{S}_i^{(c2)} \right)^{-1}. \tag{85}$$

The above procedure constrains the inertia of statistical configuration, which may cause unintended rotational momentum of $\mathbf{S}_i$ in each supercell. According to Eq. (70), we can renormalize the atomistic position vector $\mathbf{S}_i$ and cell deformation tensor by any rotational shape tensor. We therefore apply the following constraint to eliminate rotational momentum of atoms in the statistical configuration [54],

$$\mathbf{L}_\alpha = \sum_{i \in \alpha} m_i \mathbf{S}_i \times \dot{\mathbf{S}}_i, \tag{86}$$

$$\boldsymbol{\omega}_\alpha = (\mathbf{J}_\alpha^S)^{-1} \mathbf{L}_\alpha, \tag{87}$$

$$\dot{\tilde{\mathbf{S}}}_i = \dot{\mathbf{S}}_i - \boldsymbol{\omega}_\alpha \times \mathbf{S}_i, \tag{88}$$

where, $\mathbf{L}$ and $\boldsymbol{\omega}_\alpha$ are the instantaneous angular momentum and the corresponding angular velocity, respectively.

To this end, we have provided a complete computational algorithm for the constrained multiscale molecular dynamics.

5. Validation and numerical examples

To validate the proposed MMMD method, we use it to simulate the structure phase transition of single crystal Nickel and Fe.

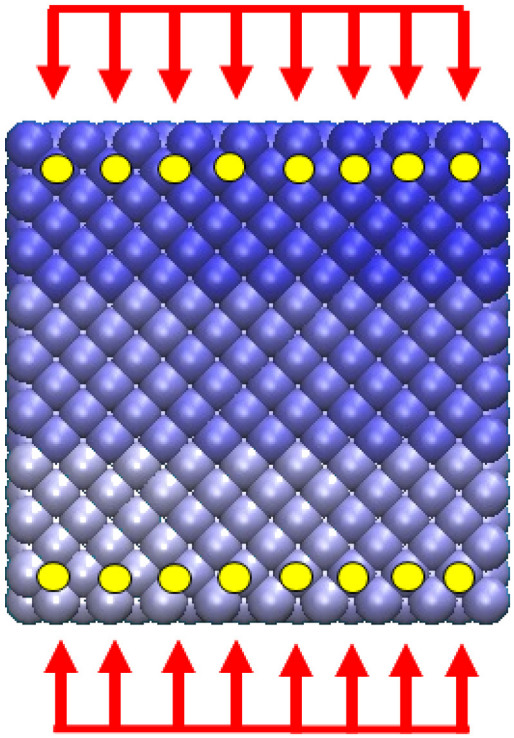

Fig. 6. Uniaxial compression of a finite size (nanoscale) nickel particle: The external load is applied by using a macroscale boundary condition, i.e. prescribing the displacement of the centers of mass of the boundary cells (yellow dots).

5.1. Structure phase transition of single crystal Ni

In the first example, we apply MMMD to simulate structure phase transition of Nickel, which was also used as the validation example for PR-MD [28]. Different from the example in [28], the validation test is done in a finite size specimen without imposing periodic boundary condition.

By imposing an uniaxial compression load, the original FCC lattice of single crystal Nickel will go through structure change [55] as shown in Fig. 6. The compression load is applied to the centers of mass of the boundary MD cells. The interaction between atoms is modeled by the Morse potential,

$$\phi(r) = D(e^{-2\alpha(r-r_0)} - 2e^{-\alpha(r-r_0)}). \tag{89}$$

The interaction force is given by

$$F(r) = -\frac{\partial \phi(r)}{\partial r} = 2D\alpha(-e^{-2\alpha(r-r_0)} + e^{-\alpha(r-r_0)}), \tag{90}$$

with the parameter constants chosen as $D = 3.5059 \times 10^{-20}$ J, $\alpha = 8.766/a_0$ and $r_0 = 0.71727$ Å. a_0 denotes the constants of the FCC lattice of Nickel, i.e. $a_0 = 3.52$ Å [28], with which the single crystal Nickel particle is in a global elastic energy minimum state. Therefore the initial starting of the test is a stable equilibrium state, which is internal stress free. The atomic weight of Nickel atom is 58.69 u.

All of simulations are carried out by using an in-house parallel computer code written in Fortran. For the microscale calculation, the reversible NVT integrator [56] was implemented for time integration, and temperature was controlled by using the Nosé-Hoover thermostat [57,58]. In the case of the mesoscale computation, the Gear six-order predictor–corrector [59] was used. Contrarily, coarse-scale integration was accomplished by using velocity Verlet algorithm with velocity scaling method as thermostat [59]. Time intervals for microscale, mesoscale and coarse-scale are set to 0.1, 1.0 and 10.0 [fs], respectively. Note that for the mesoscale and coarse scale calculations, we need additional integration procedures compared with the conventional MD simulation. However, the first Piola–Kirchhoff

stress in Eq. (67) and interaction force between supercells in Eq. (66) can be evaluated by using interatomic forces which have already been calculated in microscale time integration. Therefore, the computational efficiency of MMMD is basically comparable with that of the conventional MD, or at least at the same order of magnitude.

In the simulation, we set the temperature higher than room temperature to create an environment favorable to structure phase transition. The temperature is controlled by re-scaling the atom velocity in each MD cell at every micro time step, so that the kinetic temperature is controlled at 350 K. Before the calculation, random perturbation of positions and velocities were assigned to each atom to ensure an equilibrium state at the desired temperature. In simulations, we have constructed three different cell partitions: (1) each micromorphic cell contains $3 \times 3 \times 3 = 27$ unit cells; (2) each micromorphic cell contains $4 \times 4 \times 4 = 64$ unit cells, and (3) each micromorphic cell contains $5 \times 5 \times 5 = 125$ unit cells, and in each coordinate direction there are 3 or 5 micromorphic cell (supercell). We have two types of simulation systems: $3 \times 3 \times 3 = 27$ micromorphic cells and $5 \times 5 \times 5 = 125$ micromorphic cells. For both systems, there is one internal micromorphic cell at the center of the simulation system, with which we investigate its phase transformation process. Since each micromorphic cell or supercell contains either 27, 64, or 125 FCC unit cells, the simulation model may have different numbers of FCC unit cells ranging from 729 to 15 625 FCC unit cells. We know that each unit cell of a FCC lattice has four atoms, hence the total number of atoms in the whole simulation system ranges from 2916 atoms to 62 500 atoms.

In the simulation, we first prescribed displacement boundary condition on the centers of mass of the boundary cells by compressing the molecular system on [100] direction. Note that we do not prescribe displacement for individual atoms, but only prescribe the displacement of the centers of mass of the top and the bottom boundary MD cells. There are either $2 \times 9 = 18$ of them or $2 \times 25 = 50$ of them. By doing so, it is equivalent to prescribe the coarse scale deformation gradient $\mathbf{F}_\alpha$ close to the two boundary surfaces. Subsequently, we can control the coarse scale stretch λ_1 at the loading boundary of the simulation system at the specified value. By doing so, we can gradually make the stretch state, λ_1, of all MD cells, at boundary as well as in the interior, to the value $\lambda_1 \approx 0.7$ by compressing the displacements of the COMs of the boundary cells. During the load steps, the other components of $\mathbf{F}_\alpha$ may change according to complicated atomistic interaction, and as the prescribed boundary condition, we only control the principal stretch in [100] direction as the load parameter. Fig. 7 displays the snapshots of deformation process of Nickel block, and it also reveals the history of lattice structure change of the center MD cell. Note that the zoom-in picture is the center MD cell.

When the stretch is relatively small, i.e. $0.93 < \lambda_1 < 1$, the Nickel block is going through some elastic deformations. The particles deform uniformly. This is even true for much large stretch in infinite lattices. Since the MD simulation domain has finite size, boundary effects will inevitably influence the overall pattern of deformation. Therefore, when $\lambda \approx 0.925$, there is lattice glide or slip initiating at the lateral boundary of the system. It may be noted that PR-MD does not or cannot predict lattice slip when it simulates phase transform in an infinite lattice.

After slip or dislocation motion, the lattice structure start to change at boundary. As the principal stretch decreases from $\lambda \approx 0.82$ to $\lambda \approx 0.7$, the structure will undergo dramatic structure change, and settles a new stable state other than the initial configuration as shown in Figs. 7 and 8.

Since the major concern here is the structure phase transform of the center supercell, which is laterally confined by boundary cells, we plot the deformation sequence of MMMD simulation system in Figs. 7 and 8 to show the non-equilibrium transient process. The deformation and lattice structure change process in the center cell are shown in the small zoom-in box in Figs. 7 and 8.

We have found that the center supercell is going through several stages of elastic deformation ($\lambda_{[100]} = 1$–0.7), and then some close packed planes of {010} are gradually formed. When $\lambda_{[100]} = 0.9$–0.8, the relative positions of atoms are hold between different planes. Finally, dislocations start to form between those close packed planes, and we observed that some interplanar slips, in order to achieve a new stable position ($\lambda_{[100]} = 0.8$–0.7), and the stable lattice structure pattern is an HCP structure.

Zooming into the deformed lattice microstructure and comparing it with the initial lattice structure, we can see clearly that the lattice structure changes from FCC to HCP. The phase transition occurs when principal stretch reaches to the critical value: $\lambda_{[100]} \approx 0.7$, which is an optimal stretch to form a HCP lattice. Under the compression, the bond angle between two Nickel atoms changes from 90° to 60° while the bond length hold fixed. The original {010} plane of FCC lattice turned into the close packed plane {001} of HCP. Thus the stretch can be calculated by $\lambda_{[100]} = a_0/\sqrt{2}a_0 \approx 0.7$, which is consistent with the result in our simulation.

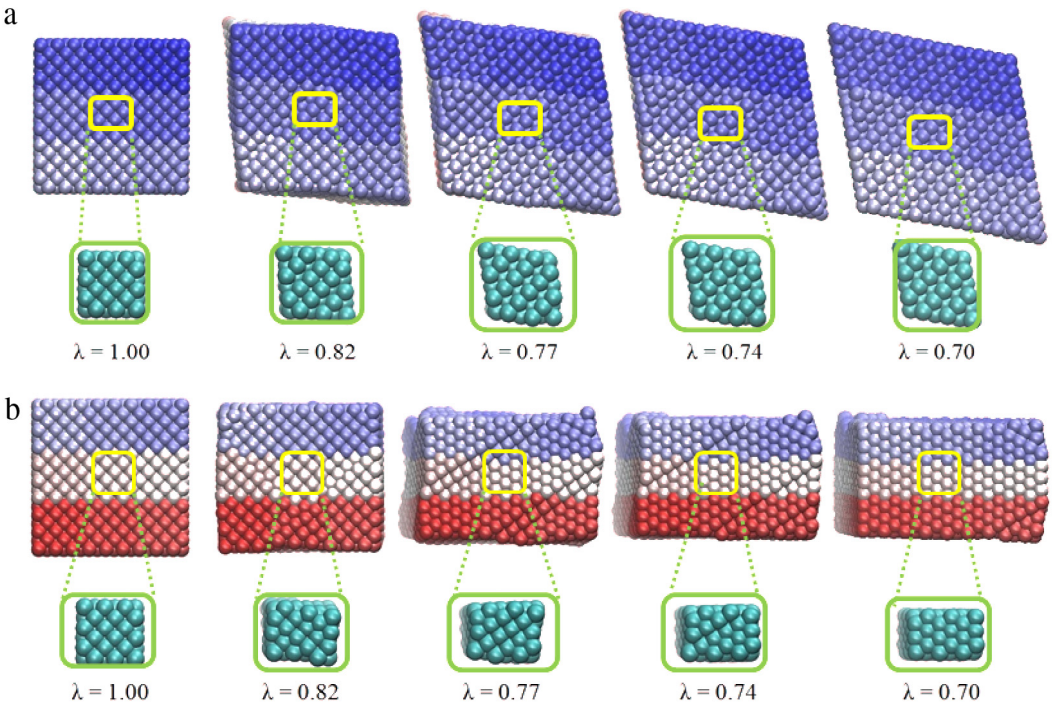

Fig. 7. Deformation and structure transition history: (a) (100) plane (top view), and (b) (010) plane (side view).

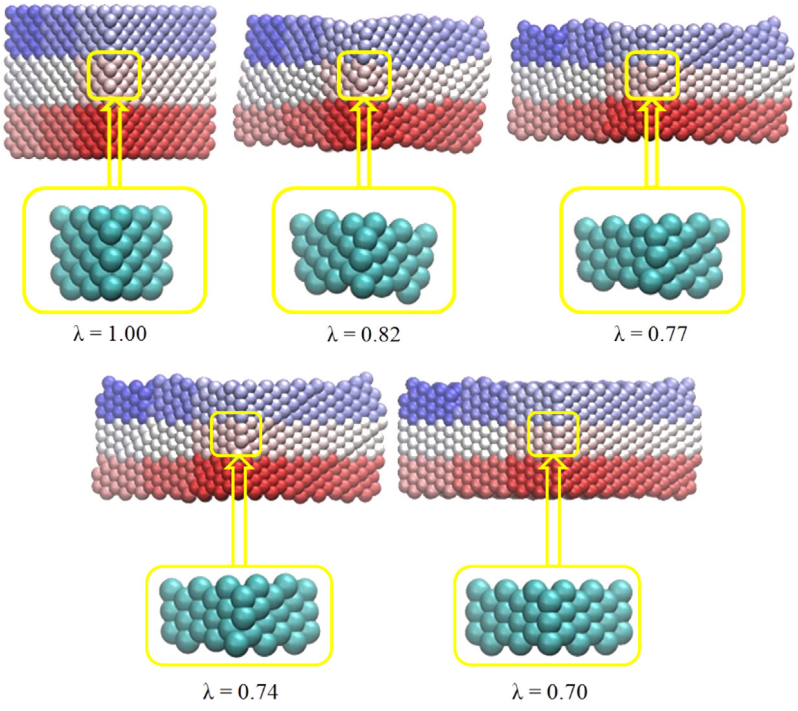

Fig. 8. Deformation and structure transition history at the corner of (010)-plane and (001)-plane (along [100]-axis).

Fig. 9 displays the supercell configurations and structures, which are represented by the total deformation gradient $\boldsymbol{\phi}_\alpha$ and the positions of the center of mass of the supercell $\mathbf{r}_\alpha$. It is possible to see visually that every cells change their shape from cubic to distorted diamond shaped hexahedron with decreasing the stretch ratio λ. Our method

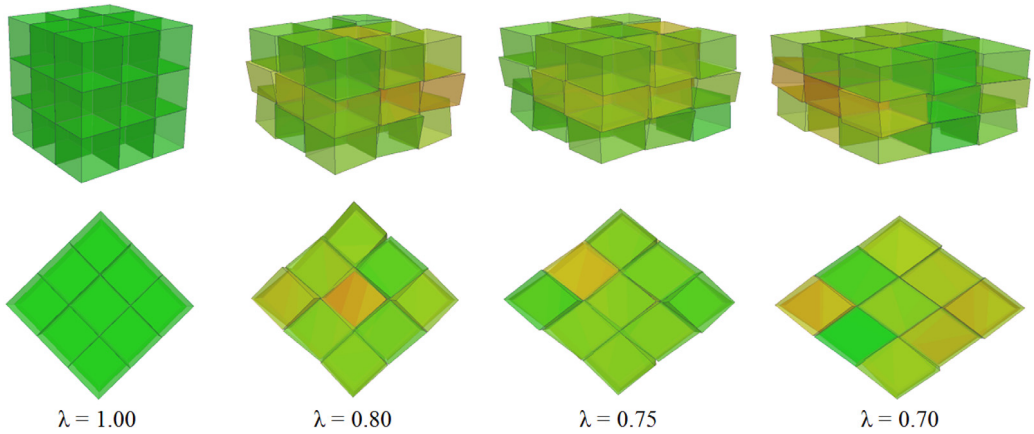

Fig. 9. Visualization of cell structures during transition of Ni.

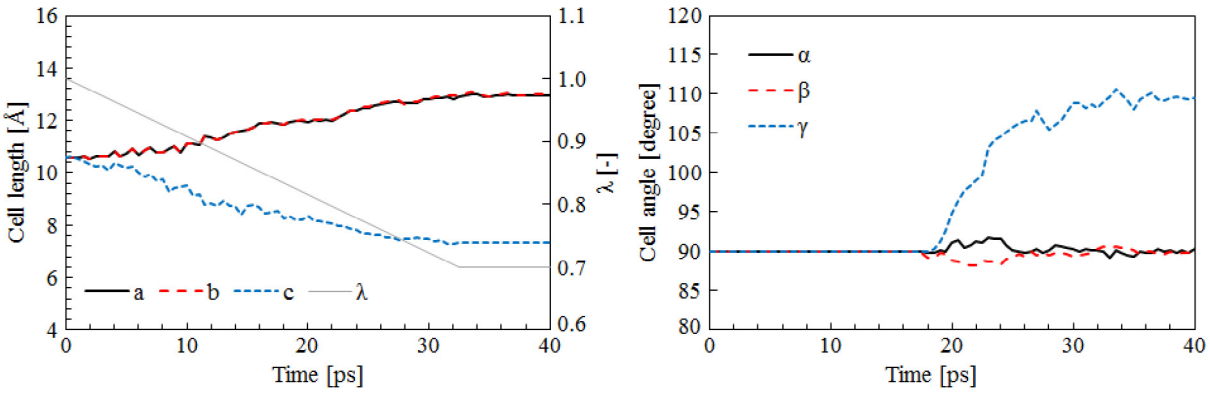

Fig. 10. Time series of cell lengths of the center cell in 3 × 3 × 3 system of Ni during the transition.

enables us to recognize local deformation by the individual deformation tensor, that distinguished MMMD from conventional MD. We can also find that the unit cells are allowed to be overlapped each other as schematically shown in Fig. 3. Fig. 10 displays a time series of edge lengths and angles of the center cell of the 3–3–3 system during this phase transition. This result clearly demonstrates the validity of the proposed algorithm, which employs Lagrangian multipliers to control cell shape i.e. Eqs. (75)–(85), can properly adjust the configurations of every supercells. As a result, scaled atom position vectors of every Si atoms are well confined within −0.5 to 0.5 (Fig. 11). We therefore conclude that the algorithm, which adopts Lagrangian multipliers to prescribe additional constraints to the total degrees of freedom, is appropriate.

Different from the APR-MD simulation, which is an equilibrium ensemble MD simulation with the prescribed constant stress, MMMD is a type of non-equilibrium molecular dynamics that can be used to calculate the non-uniform stress distribution at different locations.

By using MMMD, we are able to find the stress variation among the cells, which indicates the non-equilibrium stress state evolution inside the crystal specimen. To illustrate the MMMD's capacity to capture non-equilibrium state of the MD system, we investigated the inhomogeneous stress distribution inside the simulation system. Fig. 12(a) shows the axial stress σ_{11} distribution in re-normalized unit for each local cell, where the stress distribution is in (010)-plane.

One can see that the compressive stress is high in the middle of the specimen, and it gradually decreases towards outside. Fig. 12(b) is a smoothed distribution of stress field by numerical interpolation. However, this graph only provides a general trend of stress distribution. To obtain continuum stress distribution, a large system with more cells is needed. To quantitatively assess the accuracy of MMMD simulation, we have studied the stress–strain relation of the center supercell cell, and compared it with both Refs. [55] and [28]. The quantitative comparisons with [55]

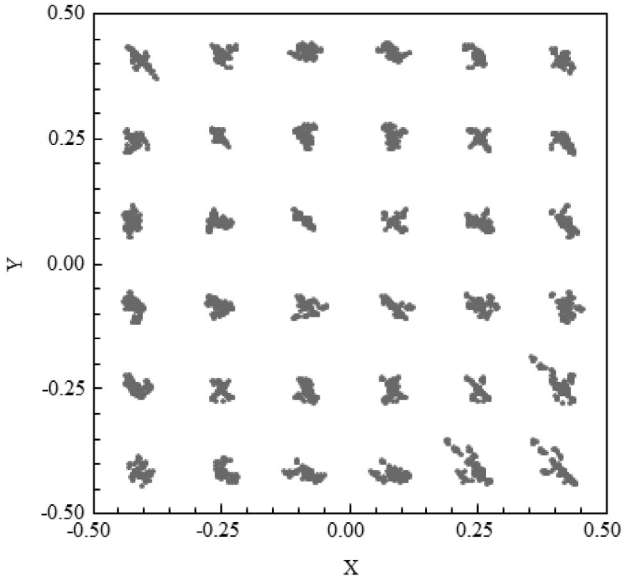

Fig. 11. Trajectories of statistical configurations of atoms in the center cell of 3 × 3 × 3 system of Ni during the transition.

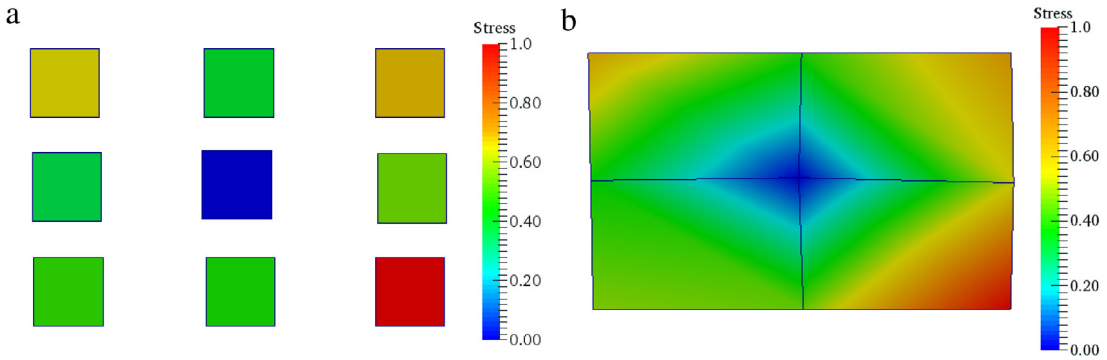

Fig. 12. Non-uniform stress distribution (σ_{11}): (a) σ_{11} in each supercell at horizontal surface, and (b) The smoothed global stress field.

and [28] are displayed in Fig. 13. Our simulation results show that the calculated critical stress value of the phase transition is almost the same as that of the infinite lattice, and it seems that MMMD provides more accurate prediction on the bifurcation of the primary and secondary load–deflection paths than that of PR-MD.

Fig. 13 also demonstrates size effects of the total system and supercell. Since all models show almost the same stress in the range from 0.9 to 1.1 of λ, we may conclude that the smallest supercell composed of 3 × 3 × 3 unit cells is large enough to capture the phase transition. Supercell size of MMMD might be insensitive if the cell contain sufficient number of atoms to represent the crystal structure and first Piola–Kirchhoff stress in Eq. (57).

5.2. *Structure phase transition of single crystal Fe*

In the second example, we apply MMMD to simulate structure phase transition of a single crystal BCC Fe to FCC structure under uniaxial loading. The structure phase transition of single crystal iron from BCC structure to FCC structure under the uniaxial tension in [0 0 1] direction is first reported by Clatterbuck et al. [60] based on an observation from ab initio calculations. This was lately confirmed by Zeng [61] who conducted a coarse grained MD field theory simulation.

In the MMMD simulation, we used the same geometry and the size that are reported in [61]. The test specimen is a single crystal iron nanorod, with two different sizes: (1) 3 × 3 × 11 supercells, and (2) 5 × 5 × 21 supercells. Each supercell contains 3 × 3 × 3 BCC unit cells with two atoms per unit cell, so that total number of atoms are 5346 and

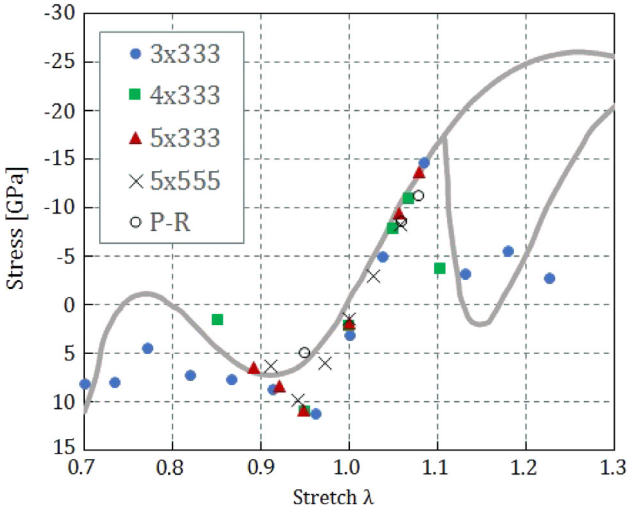

Fig. 13. Load–deflection path: σ_{11} vs. the principal stretch λ_1 for a nanoscale Nickel block under structure phase transition during the compression–tension test.

28 350, respectively. The both macroscale traction as well as macroscale displacement boundary conditions are used in the simulation, i.e we prescribe either traction or displacement at the centers of mass of $2 \times 9 = 18$ and $2 \times 25 = 50$ supercells at the two ends of the Fe nanorod for $3 \times 3 \times 11$ supercells, and (2) $5 \times 5 \times 21$ supercells, respectively.

In this simulation, we adopt the Finnis–Sinclair Model [62] for material BCC iron. The potential energy of the Finnis–Sinclair Model (FSM) and the Embedded Atom Model (EAM) has the following general form:

$$U = \frac{1}{2}\sum_{i=1}^{N}\sum_{j=1} V(r_{ij}) + \sum_{i=1}^{N} F(\rho_i) \tag{91}$$

where $F(\rho_i)$ is a functional describing the energy of embedding an atom into the background electron cloud, and it is defined as

$$\rho_i = \sum_{j\neq i}^{N} \rho(r_{ij}), \qquad \mathbf{r}_{ij} = \mathbf{r}_i - \mathbf{r}_j, \quad r_{ij} = |\mathbf{r}_{ij}|. \tag{92}$$

The Finnis–Sinclair potential is defined as

$$V(r_{ij}) = (r_{ij} - c)^2(c_0 + c_1 r_{ij} + c_2 r_{ij}^2), \qquad \rho(r_{ij}) = (r_{ij} - d)^2 + \beta\frac{(r_{ij} - d)^3}{d}, \qquad F(\rho_i) = -A\sqrt{\rho_i}, \tag{93}$$

with parameters c_0, c_1, c_2, c, A, d, and β taken from [63]. Note that both c and d are cutoff distances.

The results of MMMD simulation confirmed the previously reported results as shown in Fig. 14. In the case of traction force boundary condition, it can be observed that before the necking of the nanorod both twinning and dislocation occurred as the tensile strain increasing, and then FCC structure domain occurs at the necking region before the specimen breaks into two parts. On the other hand, clear phase transition was not observed in the simulation by using prescribed displacement boundary condition. To confirm size dependency, we also computed a larger system using $5 \times 5 \times 21$ supercells with traction force boundary condition. Fig. 15 clearly shows the phase transition from BCC structure to FCC structure around the neck, just before the Fe crystal is breaking off. According to these results, we find that an appropriate boundary condition is necessary to reproduce desired phase transition phenomena reported in the literature. It is relatively easy for MMMD to apply both displacement and traction force boundary conditions on the cell center position, and it is one of the advantages of this method.

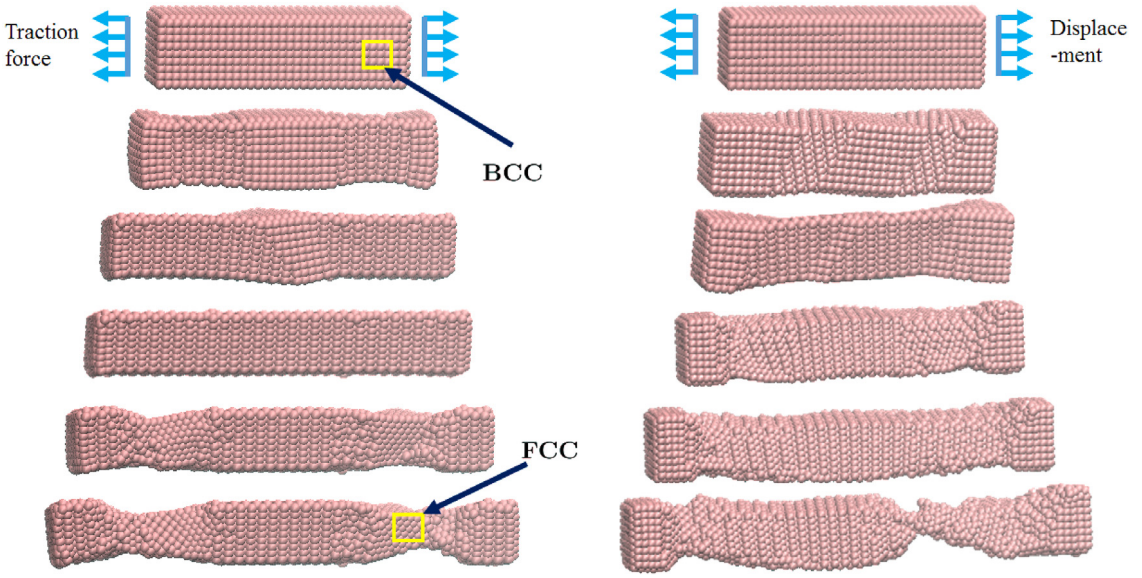

Fig. 14. Snapshots of single crystal nanorod undergoes structure phase transition from BCC to FCC during uniaxial tension. $3 \times 3 \times 11$ supercells. (Left) Traction force boundary condition, (right) displacement boundary condition.

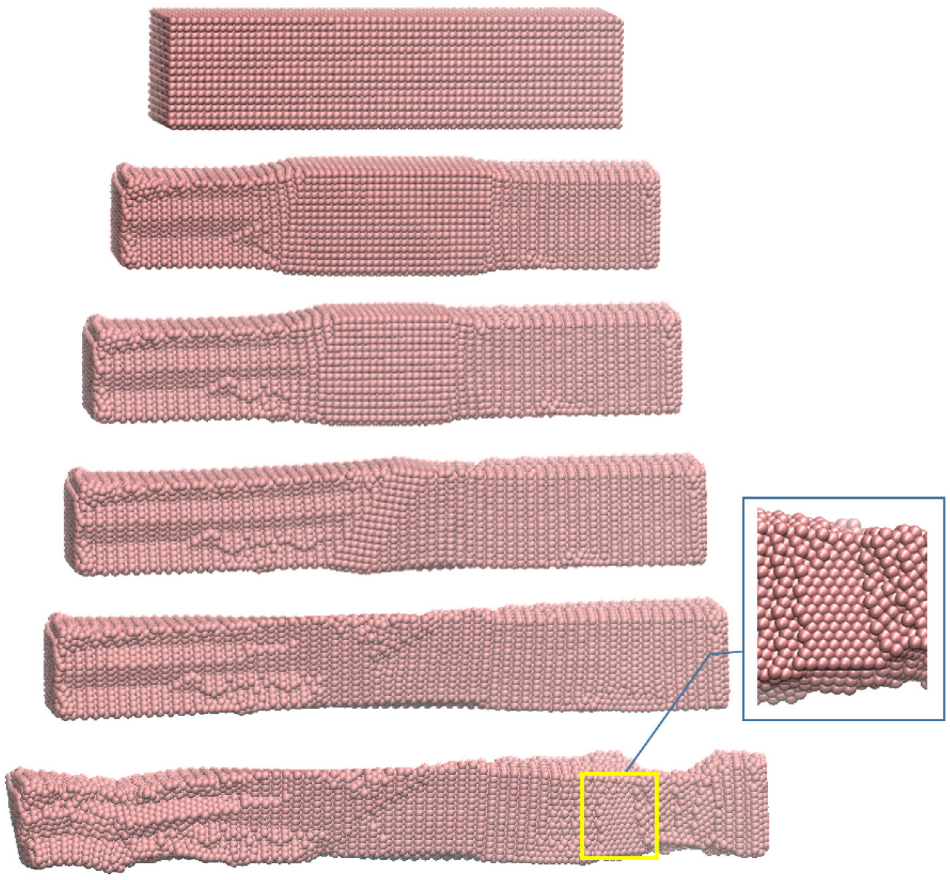

Fig. 15. Snapshots of single crystal nanorod undergoes structure phase transition from BCC to FCC during uniaxial tension. $5 \times 5 \times 21$ supercells.

6. Discussions

The main objectives of this work are: (I) Understand the inherent multiscale structure and statistical representation in conventional molecular dynamics, which can help us (A) Extrapolate statistical information from microscale molecular dynamics simulations; (B) Device better and more accurate multiscale method. It is true that the three-scale multiscale molecular dynamics does not save computer resource comparing with the conventional molecular dynamics, because it is exactly the same as the conventional molecular dynamics except that we choose a set of particular partition or sampling decomposition form to look at it. However, the outcome of this research will lay a solid theoretical foundation for developing other computer resource-saving multiscale method. For instance, we can develop a multiscale method based on presented MMMD method, in which we may use all three scales (the full version of MMMD) at the place where the defect is initiated, while using the coarse simulation only at the place that we deem less interesting. Because all three scale dynamics are intrinsically coupled, the multiscale coupling can be potentially better than some of present multiscale methods; and (II) The most significant aspect of this work, we believe, is that this work can serve as the theoretical formulation for the molecular dynamics that allows macroscale boundary condition is being applied. In near future, one may be able to apply this type of molecular dynamics solving macroscale engineering problems, or use it in engineering design of macroscale devices and machines.

The conventional wisdom assumes that if we can increase the size of molecular dynamics system we can always simulate the motion of a macroscale object by directly using first principle based molecular dynamics. This is simply not true, because when we are solving a macroscale engineering problem, we never specify the boundary conditions for each atom. In order to capture thermodynamics responses of a finite size molecular system at continuum scale, we must apply macroscale boundary conditions and initial conditions of continuum mechanics to the molecular system. If we hope that in one day we can replace some macroscale phenomenological models with the molecular dynamics model in engineering design, we must first be able to apply macroscale boundary conditions to molecular systems, and solve the problem accordingly. This requires introducing domain decomposition or domain partition that can represent non-uniform thermodynamics field variable distributions in a non-equilibrium state setting which is the statistical manifestation of microscale motions of atoms. In other words, the molecular system's thermodynamics characters must be carefully taken into account so that the microscale quantities can be correctly related to mesoscale and macroscale quantities based on first principle.

For example, in continuum mechanics, when we solve macroscale mechanics boundary value problems, we need to impose boundary conditions that are either related to traction (stress) or displacements (strain) or some other macroscale thermodynamics variables such as temperature or electrical voltage, etc. If we wish to use molecular dynamics to simulate the same macroscale problem based on first principle, we must be able to apply the same type of boundary conditions, which have to be consistent with macroscale engineering measurements, to first principle based molecular dynamics. As computer and computing technology progress, the need for direct first principle molecular dynamics solution of macroscale problems will become more and more relevant, important, and urgent. Thus, we should develop a rigorous multiscale molecular dynamics that can take this task, i.e. a molecular dynamics that can couple macroscale thermodynamic variables with microscale atomic variables from first principle rather than directly couple molecular dynamics with the existing phenomenological continuum mechanics by superficial boundary matching or blending.

In this work by utilizing the local equilibrium assumption, we have extended the equilibrium (Andersen)-Parrinello-Rahman molecular dynamics to a non-equilibrium atomistic-to-continuum dynamics, which can compute the motions of a finite size molecular system subjected arbitrary macroscale boundary conditions instead of periodic boundary condition or the boundary condition on specific atoms. The application of macroscale boundary condition to a molecular system is not a trivial task, both theoretically as well as computationally. The so-called macroscale boundary condition may alternatively be called as the thermodynamics flux boundary condition, such as heat flux (temperature), linear momentum flux (force), mass flux (diffusion), energy flux (material force) boundary conditions, etc. Therefore, when prescribing the flux boundary condition to a molecular system, small or large, we are simulating a non-equilibrium problem. In fact, this has been one of the crucial parts in non-equilibrium molecular dynamics simulation. For example when using non-equilibrium MD to simulate fluids, a common flux boundary condition used is called the Lees–Edwards Boundary condition (see [64]), which is a macroscale displacement boundary condition for fluid boundary, but it is limited in periodic setting, whereas the macroscale boundary condition discussed in this paper is much more general and systematical. Moreover, the common belief on the difference between microscale

molecular systems and macroscale continuum systems is that microscale system has a small size (small length scale), and macroscale system has a large size (large length scale). However, a profound difference between the two is that the microscale system is usually (not always) in an equilibrium state whereas the macroscale system is most likely (not always) in a non-equilibrium state, which is the essence of multiscale simulation, and the macroscale boundary condition plays a key role in this matter.

Finally, in this work, we proposed in the first time a novel computational algorithm for multiscale micromorphic molecular dynamics that is based on the novel concept of the multiplicative multiscale decomposition. The proposed MMMD computational algorithm not only separates but also couples macroscale continuum deformation with discrete atomistic motions, so that we can apply MMMD to solve engineering problems with general thermodynamics boundary conditions in finite size region under non-equilibrium condition. The essence of multiscale molecular dynamics computation is not just saving computational resource, but rather conducting simulation of non-equilibrium systems, because most systems in macroscale are non-equilibrium thermodynamics systems. The approach adopted in this work is to utilizing the so-called local equilibrium assumption (LEA), so that we may assume that each cell in a short period is in an equilibrium state, so that we can conduct an incremental and local PR-MD simulation. In the next time cycle, the cell may change to a new equilibrium state, and by integrating all three scales together, we piece together a complete picture of a non-equilibrium thermodynamic process.

The MMMD formulation is basically a global partition of first principle molecular dynamics Lagrangian into a set of local Lagrangian of NσH equilibrium ensembles for solids. A future study is to extend the present MMMD formulation to other local equilibrium ensembles of molecular dynamics such as local NσT ensemble.

Acknowledgment

Dr. S. Urata is sponsored by Asahi Glass Co., Ltd., Japan, and this support is greatly appreciated.

References

[1] J. Dongarra, The international exascale software project roadmap, Int. J. High Perform. Comput. Appl. 25 (2011) 3–60.
[2] M. Berkowitz, J.A. McCammon, Molecular dynamics with stochastic boundary conditions, Chem. Phys. Lett. 90 (1982) 215–217.
[3] C.L. Brooks Iii, M. Karplus, Deformable stochastic boundaries in molecular dynamics, J. Chem. Phys. 79 (1983) 6312–6325.
[4] F. Cleri, S.R. Phillpot, D. Wolf, S. Yip, Atomistic simulations of materials fracture and the link between atomic and continuum length scales, J. Am. Ceram. Soc. 81 (1998) 501–516.
[5] F. Cleri, Representation of mechanical loads in molecular dynamics simulations, Phys. Rev. B 65 (2001) Article 014107.
[6] C. Schäfer, H.M. Urbassek, L.V. Zhigilei, B.J. Garrison, Pressure-transmitting boundary conditions for molecular-dynamics simulations, Comput. Mater. Sci. 24 (2002) 421–429.
[7] R.E. Rudd, J.Q. Broughton, Coarse-grained molecular dynamics and atomic limit of finite elements, Phys. Rev. B 58 (1998) R5893–R5896.
[8] G.J. Wagner, W.K. Liu, Coupling of atomistic and continuum simulations using a bridging scale decomposition, J. Comput. Phys. 190 (2003) 249–274.
[9] S.P. Xiao, Ted Belytschko, A bridging domain method for coupling continua with molecular dynamics, Comput. Methods Appl. Mech. Engrg. 193 (2004) 1645–1669.
[10] A.C. To, S. Li, Perfectly matched multiscale simulations, Phys. Rev. B 72 (2005) Article No. 035414.
[11] H.S. Park, E.G. Karpov, W.K. Liu, Non-reflecting boundary conditions for atomistic, continuum and coupled atomistic/continuum simulations, Internat. J. Numer. Methods Engrg. 64 (2005) 237–259.
[12] E.G. Karpov, H. Yu, H.S. Park, W.K. Liu, Q.J. Wang, D. Qian, Multiscale boundary conditions in crystalline solids: theory and application to nanoindentation, Int. J. Solids Struct. 43 (2006) 6359–6379.
[13] S. Namilae, D.M. Nicholson, P.K.V.V. Nukala, C.Y. Gao, Y.N. Osetsky, D.J. Keffer, Absorbing boundary conditions for molecular dynamics and multiscale modeling, Phys. Rev. B 76 (2007) Article No. 144111.
[14] R.E. Miller, E.B. Tadmor, A unified framework and performance benchmark of fourteen multiscale atomistic/continuum coupling methods, Modelling Simulation Mater. Sci. Eng. 17 (2009) Article No. 053001.
[15] S. Li, X. Liu, A. Agrawal, A.C. To, Perfectly matched multiscale simulations for discrete systems: Extension to multiple dimensions, Phys. Rev. B 74 (2006) 045418.
[16] J. Li, D. Liso, S. Yip, Coupling continuum to molecular-dynamics simulation: Reflecting particle method and the field estimator, Phys. Rev. E 57 (1998) 7259–7267.
[17] R.E. Rudd, J.Q. Broughton, Atomistic simulation of MEMS resonators through the coupling of length scales, J. Model. Simul. Microsyst. 1 (1999) 29–38.
[18] Y. Chen, J.D. Lee, Connecting molecular dynamics to micromorphic theory. (I). Instantaneous and average mechanical variables, Physica A 322 (2003) 359–376.
[19] R.E. Rudd, J.Q. Broughton, Coarse-grained molecular dynamics: nonlinear finite elements and finite temperature, Phys. Rev. B 72 (2005) 144104.

[20] X. Liu, S. Li, Nonequilibrium multiscale computational model, J. Chem. Phys. 126 (2007) article No. 124105.
[21] X. Li, A coarse-grained molecular dynamics model for crystalline solids, Internat. J. Numer. Methods Engrg. 83 (2010) 986–997.
[22] Y. Chen, J.D. Lee, Connecting molecular dynamics to micromorphic theory. (II). Balance laws, Physica A 322 (2003) 377–392.
[23] Y. Chen, Reformulation of microscopic balance equations for multiscale materials modeling, J. Chem. Phys. 130 (2009) 134706.
[24] L. Xiong, G. Tucker, D.L. McDowell, Y. Chen, Coarse-grained atomistic simulation of dislocations, J. Mech. Phys. Solids 59 (2) (2011) 160–177.
[25] A.C. Eringen, Mechanics of Micromorphic Continua, Springer, 1968.
[26] H.C. Andersen, Molecular dynamics simulations at constant pressure and or temperature, J. Chem. Phys. 72 (1980) 2384–2393.
[27] M. Parrinello, A. Rahman, Crystal structure and pair potentials: A molecular dynamics study, Phys. Rev. Lett. 14 (1980) 1196–1199.
[28] M. Parrinello, A. Rahman, Polymorphic transitions in single crystals: A new molecular dynamics method, J. Appl. Phys. 12 (1981) 7182–7190.
[29] A. Laio, M. Parrinello, Escaping free-energy minima, Proc. Natl. Acad. Sci. USA 99 (2002) 12562–12566.
[30] R. Martonik, A. Laio, M. Parrinello, Predicting crystal structures: the Parrinello-Rahman method revisited, Phys. Rev. Lett. 90 (2003) 075503.
[31] R. Martonk, D. Donadio, A. Oganov, M. Parrinello, Crystal structure transformations in S_iO_2 from classical and $ab\ initio$ metadynamics, Nat. Mater. 5 (2006) 623–626.
[32] P. Podio-Guidugli, On (Andersen)-Parrinello-Rahman molecular dynamics, the related metadynamics, and the Use of the Cauchy-Born rule, J. Elasticity 100 (2010) 145–153.
[33] M.H. Ulz, Coupling the finite element method and molecular dynamics in the framework of the heterogeneous multiscale method for quasi-static isothermal problems, J. Mech. Phys. Solids 74 (2015) 1–18.
[34] M.H. Ulz, A multiscale molecular dynamics method for isothermal dynamic problems using the seamless heterogeneous multiscale method, Comput. Methods Appl. Mech. Engrg. 295 (2015) 510–524.
[35] S. Li, Q. Tong, A concurrent multiscale micromorphic molecular dynamics, J. Appl. Phys. 117 (2015) No. 154303.
[36] Q. Tong, S. Li, From molecular systems to continuum solids: A multiscale structure and dynamics, J. Chem. Phys. 143 (2015) No. 064101. http://dx.doi.org/10.1063/1.4927656.
[37] Q. Tong, Li S, A multiscale molecular dynamics allowing macroscale mechanical loads, Eur. Phys. Lett. 110 (2015) No. 60005.
[38] S. Li, W. Liu, Reproducing kernel hierarchical partition of unity. Part I: formulation and theory, Internat. J. Numer. Methods Engrg. 45 (1999) 251–288.
[39] S. Silling, M. Epton, O. Weckner, J. Xu, E. Askari, Peridynamic states and constitutive modeling, J. Elasticity 88 (2007) 151–184.
[40] E.B. Tadmor, M. Ortiz, R. Phillips, Quasicontinuum analysis of defects in solids, Phil. Mag. A 73 (6) (1996) 1529–1563.
[41] S. Li, N. Sheng, X. Liu, A non-equilibrium multiscale simulation paradigm, Chem. Phys. Lett. 451 (2008) 293–300.
[42] S. Li, N. Sheng, On multiscale non-equilibrium molecular dynamics simulations, Internat. J. Numer. Methods Engrg. 83 (2010) 998–1038.
[43] J. Marsden, T. Hughes, Mathematical Foundations of Elasticity, Prentice-Hall, Inc., 1983.
[44] J. Irving, J.G. Kirkwood, The statistical mechanical theory of transport processes. IV. The equations of hydrodynamics, J. Chem. Phys. 18 (1950) 817–829.
[45] D.H. Tsai, The virial theorem and stress calculation in molecular dynamics, J. Chem. Phys. 70 (1979) 1375.
[46] M. Zhou, A new look at the atomic level virial stress: on continuum-molecular system equivalence, Proc. R. Soc. Lond. Ser. A Math. Phys. Eng. Sci. 459 (2003) 2347–2392.
[47] A. Murdoch, A critique of atomistic definition of the stress tensor, J. Elasticity 88 (2007) 113–140.
[48] A.K. Subramaniyan, C.T. Sun, Continuum interpretation of virial stress in molecular simulations, Int. J. Solids Struct. 45 (2008) 4340–4346.
[49] M.H. Ulz, Comments on a Continuum-Related Parrinello-Rahman molecular dynamics formulation, J. Elasticity 113 (2013) 93–112.
[50] J.-P. Ryckaert, G. Ciccotti, H.J.C. Berendsen, Numerical integration of the Cartesian equations of motion of a system with constraints: Molecular dynamics of n-Alkanes, J. Comput. Phys. 23 (3) (1977) 327–341.
[51] H.C. Andersen, RATTLE: A "Velocity" version of the SHAKE algorithm for molecular dynamics calculations, J. Comput. Phys. 52 (1983) 2434.
[52] S.G. Lambrakos, J.P. Boris, E.S. Oran, I. Chandrasekhar, M. Nagumo, A modified SHAKE algorithm for maintaining rigid bonds in molecular dynamics simulations of large molecules, J. Comput. Phys. 85 (2) (1989) 473486.
[53] L. Verlet, Computer "experiments" on classical fluids. I. Thermodynamical properties of Lennard-Jones molecules, Phys. Rev. 159 (1967) 98103.
[54] Y. Zhou, M. Cook, M. Karpus, Protein motions at zero-total angular momentum: The importance of long-range correlations, Biophys. J. 79 (2000) 2902.
[55] F. Milstein, B. Farber, Theoretical fcc–bcc transition under [100] tensile loading, Phys. Rev. Lett. 44 (1980) 277–280.
[56] G.J. Martyna, M.E. Tuckerman, D.J. Tobias, M.L. Klein, Explicit reversible integrators for extended systems dynamics, Mol. Phys. 87 (5) (1996) 1117.
[57] S. Nosé, A unified formulation of the constant temperature molecular dynamics methods, J. Chem. Phys. 81 (1984) 511.
[58] W.G. Hoover, Canonical dynamics: Equilibrium phase-space distributions, Phys. Rev. A 31 (1985) 1695.
[59] D. Frenkel, B. Smit, Understanding Molecular Simulation from Algorithm to Applications, Academic press, 1996.
[60] D.M. Clatterbuck, D.C. Chrzan, J.W. Morris Jr., The ideal strength of iron in tension and shear, Acta Mater. 51 (2003) 2271–2283.
[61] X. Zeng, Application of an atomistic field theory to Nano/Micro materials modeling and simulation, CMES Comput. Model. Eng. Sci. 74 (2011) 183–201.
[62] M.W. Finnis, J.E. Sinclair, A simple empirical N-body potential for transition metals, Phil. Mag. A 50 (1) (1984) 45–55.
[63] M.W. Finnis, J.E. Sinclair, Erratum: A simple empirical N-body potential for transition metals, Phil. Mag. A 53 (1) (1986) 161.
[64] A.W. Lees, S.F. Edwards, The computer study of transport processes under extreme conditions, J. Phys. C: Solid State Phys. 5 (15) (1972) 1921.